Modification of morphologies and mechanical properties of Si crystal by low fluence ion beam irradiation in sub-micrometer scale

Xiaowei Guo

Department of Mechanical Systems Engineering,

Kochi University of Technology

March 6, 2015

Abstract:

The importance of complicated 3-dimensional (3-D) structure in micro or nanometer scale is increasing in various fields, such as electric device, micro-electromechanical systems (MEMS), optical devices and biochips. In addition to a geometric shape of the surface, mechanical properties are also important factors to be considered, especially in the field of MEMS. However, it is difficult to fabricate such complicated 3-D structures with satisfying mechanical properties by means of conventional method. Ion-beam technologies, used to be applied as a useful and convenient tool to fabricate 2-D structures in nanometer scale, is one of hopeful candidates by expanding its ability to 3-D fabrication because of its high resolution along lateral direction and a controllability of its projection range. Recently, it has been confirmed that an expansion effect of crystal material by irradiating relatively low-fluence ion-beam causes a surface swelling, and the swelling height could be controlled by irradiation parameters. If this expansion effect is applied to fabrication of 3-D micro-/nanostructures, it is expected that morphological modification of micro/nanostructure can be achieved without serious deterioration of their mechanical properties. In order to develop new fabrication method by means of the expansion effect, I intend to investigate lateral deformation of micro-/nanostructures and modification of mechanical properties of crystal materials induced by low fluence ion beam irradiation.

In this thesis, initial nanostructures with different lateral size on Si-crystal fabricated by focused ion beam (FIB) were irradiated by 240 keV Kr beam with fluence up to 5×10^{14} ion/cm^2. Lateral deformation of nanostructures has been successfully achieved firstly by irradiating low-fluence ion beam and this deformation strongly depends on the fluence of irradiation and structure size of initial nanostructure. Raman spectroscopy were used to investigate evolutional behavior of amorphous fraction at the same time. Transmission electron microscopy (TEM) measurement and stopping and range of ions in matter (SRIM) calculation were utilized to evaluate inner change of crystal Si and defects distribution in irradiated crystal Si, respectively. TEM images indicated the evolution of heterogeneous amorphization, which is associated with stress in the lattice structure. The heterogeneous

amorphization can give consistent explanation to understand the fluence dependence. The suppression effect on the lateral deformation, which would be originated from crystalline region between two interfaces in the center pile, provides a possible explanation for the structure size dependence.

In addition, the mechanical properties of crystal Si irradiated by low fluence ion-beam were also investigated by nanoindentation method. Observed results indicated that both modification of hardness and that of Young's modulus depended on fluence. In addition, the hardness was more sensitive to the damage induced by ion beam irradiation than the Young's modulus. The fluence dependence of Young's modulus can be understood by the induced decrease in the order of Si network by ion beam irradiation while the fluence dependence of hardness was ascribed to the induced increase of defects caused by ion beam irradiation. The different sensitivities of modified mechanical properties to damage induced by ion beam irradiation were ascribed to their different mechanism of modification. In addition, a new method of determining the longitudinal size of phase transition region was proposed. The observed results showed the modified mechanical properties depend on the fluence. Based on the above investigations, it is expected that ion beam technology is of great potential to be applied to the fabrication of complicated 3-D nanostructures by means of expansion effect.

Contents

1 Introduction..8
1.1 Fabrication of 3D micro-/nanostructures..8
1.2 Modification of mechanical properties induced by ion-beam irradiation..10
1.3 Object of this study..11
2 Modification of Si-crystal induced by ion-beam irradiation..11
2.1 Properties of Si-crystal..12
2.2 Damage induced by ion beam irradiation..14
2.2.1 Nuclear damage and electronic damage..14
2.3 Modification of surface profile..15
2.3.1 Control of the swelling height..15
2.3.2 Control of lateral size of microstructure..18
2.4 Mechanical properties of crystalline material..20
2.4.1 Anisotropic mechanical properties of c-Si..20
2.4.2 Modification of mechanical properties..22
3 Experimental method..24
3.1 Sample's preparation..24
3.1.1 Preparation of initial nanostructure on Si crystal..24
3.1.2 Preparation of sample for nanoindentations test..25
3.2 Irradiation of samples by Kr-ion irradiation..26
3.2.1 Condition of irradiation..26
3.2.2 Selection of charge state..26
3.2.3 Measurement of fluence..28
3.3 Evaluation of irradiation effect..29
3.3.1 Raman spectroscopy..29
3.3.2 Scanning electron microscopy measurement..31
3.3.3 Transmission Electron Microscope..31

3.3.4 Nanoindentation 34
3.3.5 Rutherford backscattering spectrometry channeling (RBS-C) 38
3.4 Calculation of damage distribution by SRIM 39
4 Modification of morphologies of c-Si nanostructure 42
4.1 Observation of stripe structures and nano-hole structure by SEM 42
4.1.1 Lateral deformation of nanostructures irradiated by Kr-beam 43
4.1.2 Lateral deformation as a function of fluence 43
4.1.3 Lateral deformation as a function of structural size 46
4.2 Observation of Raman spectrum 48
4.2.1 Raman spectrum observed at different fluence 48
4.2.2 Definition of amorphous fraction by using Raman spectrum 49
4.2.3 Growing behavior of amorphous nature in Si crystal 49
4.3 Observation of TEM image 50
4.3.1 Evolution of amorphous layer with fluence 50
4.3.2 Crystalline and amorphous pockets observed at interface layer 51
4.4 Mechanism of lateral deformation induced by low fluence ion beam irradiation 54
4.4.1 Contribution of sputtering effect 54
4.4.2 Comparison with irreversible deformation 54
4.4.3 Contribution of amorphous/crystalline pockets 55
4.4.4 Contribution of lateral size 55
4.5 Conclusion 56
5 Modification of mechanical properties of Si crystal 56
5.1 Measurement of mechanical properties by means of nanoindentation 57
5.2 Observation of Raman spectrum 62
5.3 Observation of TEM image 63
5.4 Measurement of RBS-C spectrum 65
5.5 Calculation of amorphous layer by SRIM 66

5.6 Effect of irradiation damage on mechanical properties 68

5.6.1 Fluence dependence 68

5.6.2 Comparison between changes in Young's modulus and hardness 72

5.6.3 The application of depth profile of mechanical properties 73

5.7 Conclusion on modification of mechanical properties 73

6 Conclusion 74

APPENDIX: 83

List of acronyms

TEM – Transmission electron microscopy

RBS-C – Rutherford backscattering-channeling

SEM – Scanning electron microscopy (microscope)

RT – Room-temperature

SRIM – the Stopping and Range of Ions in Matter

FIB – focused ion beam

1 Introduction

With the wide application such as micro-electromechanical system (MEMS) in electronic devices, drug therapy, sensors [1-4], the importance of 3-D micro-/nanostructure draws much attention in the field of micro-/nano fabrication. Ion-beam technology, as a powerful tool, can be applied in this field. However, there are still many factors to be investigated for the application of ion-beam technology to the field of micro-/nanofabrication, such as modification of morphologies on micro-/nanostructures, which is related to the controlling the size of microstructures, and modification of mechanical properties of materials, which is associated with the requirement of MEMS instruments.

1.1 Fabrication of 3D micro-/nanostructures

3-D nanostructure is the extension of 2-D nanostructure, so well-developed techniques of 2-D nanostructure fabrication are necessary to be reviewed as basis. To fabricate 2-D nanostructure, there are many conventional methods, such as optical lithography, scanning probes, nano imprinting and electron/ ion beam lithography. Optical lithography is convenient for fabricating planar micro-/nano-structures. In this technology, a mask is imaged onto a flat substrate surface coated with a thin layer of photoresist. The photon energy is focused onto the photoresist, causing cross-linking. Then the pattern of mask is delineated into the photoresist after development. The advantage of optical lithography is to deliver sub-100 nm patterning, but disadvantage is that the masks are too expansive. Different from optical lithography, scanning probes can be implemented with diverse mechanisms. Electrons emitted from a probe can expose thin polymer resist. Very high local electric field can be applied to modify the surface of a sample, such as local oxidation, thermal melting or decomposition. The deposition patterns can be formed on the sample surface by materials transported from a probe. Patterns also can be formed on the sample surface by scratching with a probe. The advantage of scanning probe method are simple, low-cost for sub-100 nm structure while the disadvantages are small region, low speed of fabrication and shallow structures in depth. Nano imprinting lithography (NIL) is simple

and of high resolution. In this technique, a pattern is transferred to the surface of a sample by simply bringing the stamp in contact with the surface. The advantages of this method are used to fabricate high-density periodical pattern but this method is limited for soft lithography. Electron/ion-beam lithography technique is similar to optical lithography. Charged particle beams deposit energy to a substrate to fabricate pattern either by removing material directly or by exposure of energy-sensitive polymer materials. Although, this technology has been applied to fabricate micro-/nanostructure for more than 40 years [5-12] and has obvious advantages such as high resolution and high flexibility, a low throughput is still a limit of its application. In summary, these conventional methods are well-developed techniques for fabricating 2-D structure. However, they cannot be directly applied to fabricate 3-D structures because of controllable requirements of structure size in vertical and lateral direction.

To fabricate 3-D nanostructures, the development of new method or procedures is needed. As one candidate of powerful tools of morphological modification to tailor materials or common nano-structure, ion-beam irradiation have played an important role in the fields of micro-/nanofabrication, so material deformation induced by ion-beam irradiation has attracted much attention.

The lateral deformation of micro-/nanostructures of amorphous silicon (*a*-Si) have been observed under the irradiation of ion-beam [13, 14] , and this phenomena was explained based on a viscoelastic and free volume model by Dillen *et al.* [13]. However, these plastic deformations require high fluence of ion-beam irradiation, which cause serious damages of mechanical properties in irradiated materials [15]. The results of plastic deformation indicate that the problems of plastic deformation in the application of micro-/nanofabrication are serious damage and poor controllability because of sputtering effect induced by high fluence ion-beam irradiation. To extend this fabrication method of more complicated structure with reducing serious damages, the expansion effect induced by low fluence ion-beam irradiation is one of the hopeful candidates. Recently, some researchers have discovered the swelling phenomenon in region where is irradiated by ion beam [16-19]

and the controllability of swelling height was experimentally confirmed in ref. [20]. The mechanism of this phenomenon is ascribed to the damage (vacancies) induced by ion-beam irradiation [16]. These results indicate that the deformation (swelling) induced by ion-beam irradiation is a simple and controllable method for the 3-D nano-structural fabrication in vertical direction. Based on these results, the lateral deformations of materials induced by ion-beam irradiation is also expected.

In the present study, to observe the lateral deformation of crystalline silicon (*c*-Si) nano-structures induced by ion-beam irradiation, Kr-ion beam with an energy of 240 keV was implanted into *c*-Si nanostructures. The induced lateral deformation was observed as the modification of a cross sectional profile of nanostructure, which was observed before and after ion-beam irradiation by high-resolution scanning electron microscopy (SEM). In addition, to understand observed lateral deformation, Raman spectroscopy and transmission electron microscope (TEM) are also utilized to evaluate the irradiation effect.

1.2 Modification of mechanical properties induced by ion-beam irradiation

The effect on tailoring materials [16, 21] or modifying surface [13, 22-25] can be conveniently controlled by means of irradiation parameters, such as energy and fluence. Ion-beam technology, as development of fabrication method, promotes its application to the fabrication of microelectromechanical systems (MEMS). In general, ion-beam irradiation induces definite modifications of mechanical properties, which are part of important requirements for MEMS, such as resonant sensor. To investigate the irradiation effect on mechanical properties, Su *et al.* [26] reported that the hardness of poly-crystalline silicon irradiated by various ions was affected by the formed bond because of the chemical effects induced by ions. In addition, the 'size effect' on mechanical properties of micro-structure is also important. Unchanged Young's modulus of crystal silicon nano-cantilever was found at a minimum thickness of 255 nm by Namazu *et al.* [27]. Virvani *et al.* [28] extended the minimum thickness of unchanged elastic modulus to 193 nm. However, a significant decrease in the elastic modulus of silicon cantilevers was reported by *Li et al.* [29], when

their thickness was reduced from 170 to 12 nm. Therefore, to investigate the irradiation effect on mechanical properties of sub-microstructures, block material irradiated with inertia ions, without an induced chemical effect, is available.

At present, although many researches related to mechanical properties of silicon materials have been reported [15, 29-31], their depth profile modified by ion-beam irradiation, which is important for micro-structures, was rarely reported. In this section, the mechanical properties were investigated on crystalline silicon (*c*-Si) samples irradiated by Kr-beam with energy of 240 keV and fluence of 1 and 5×10^{14} ions/cm^2. In order to achieve the depth profile of an irradiation effect, the continuous measurement of mechanical properties was performed by nanoindentation. Depth distribution of defects was supplied from stopping and range of ions in matter (SRIM) calculation, transmission electron microscopy (TEM) observation, and Rutherford backscattering-channeling (RBS-C) to investigate modification of mechanical properties. In addition, the comparison of change in mechanical properties for low and high fluence irradiation will be performed.

1.3 Object of this study

The objects of this study included two parts. The first one is to evaluate the modification of the morphologies of *c*-Si structure in lateral direction to confirm the controllability of this method. The second one is to investigate the irradiation effect on mechanical properties to provide basic information for supporting the application of ion-bean technology in the field of micro-/nanofabrication.

2 Modification of Si-crystal induced by ion-beam irradiation

The results of previous researches indicated that the morphological deformation of crystalline materials induced by ion-beam irradiation mainly come from the irradiation damage in crystalline silicon. Considering this damage coming from the interaction between ion and materials, the structure of crystalline Si, mechanical properties of crystalline Si, and

their modifications induced by ion-beam irradiation are explained in this section.

2.1 Properties of Si-crystal

As a kind of semiconductor material, crystalline silicon (c-Si) has many advantageous properties: high purities, the availability of large single crystals, a matching insulator and natural abundance, effective conductive engineering. All these advantageous properties ascribe to its crystalline structure and electron configuration shown in Fig. 2-1 and Fig. 2-2, respectively.

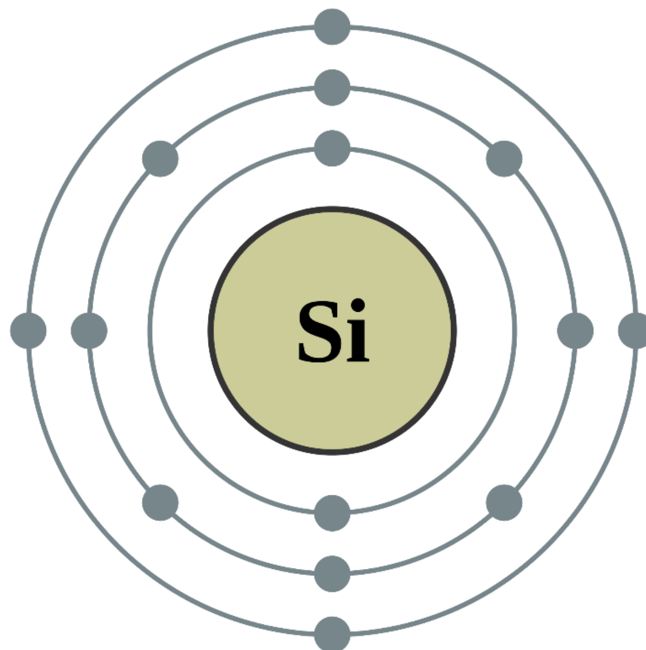

Figures. 2-1 Electron configuration of Si atom

(a) Lattice structure

The lattice of single-crystal Si is of the simplest three-dimensional lattice system referred to as the cubic lattice system. Any lattice system having a cubic volume as a unit cell belongs to the cubic family. The size of the unit cell is defined by the lattice constant a, as shown in Fig. 2-2. *c*-Si has a cubic lattice structure called the diamond lattice structure and the lattice constant for Si is 5.43 Å. Although bulk Si is an ideal lattice comprised of an infinite number of repetitive unit cells, there are several primary planes and lattice directions that are

associated with the unit cell. These primary planes are those that form the sides and diagonals of the unit cell.

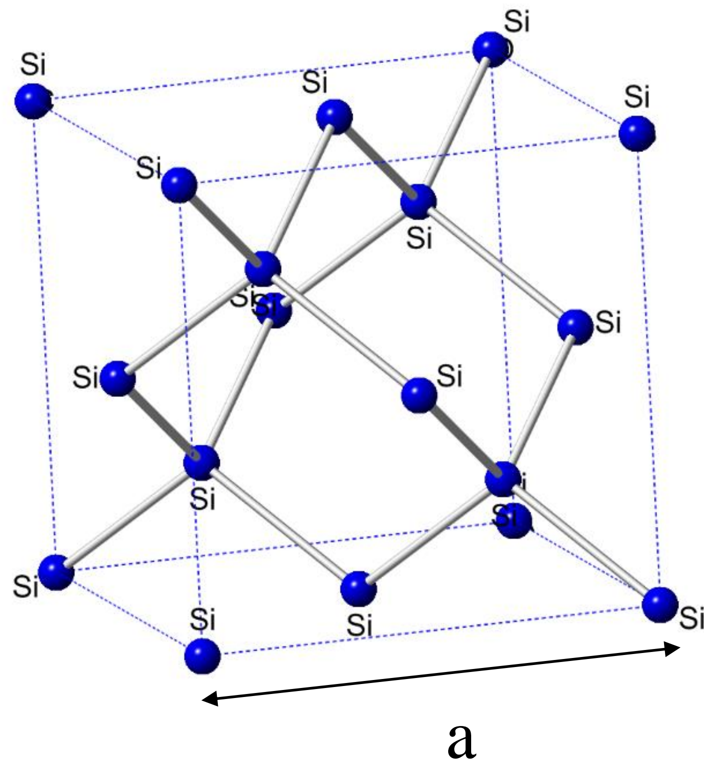

Figures. 2-2 crystalline structure of Si. Dotted lines indicate unit cell

(b) Miller indices and crystal planes

Miller indices are used to describe all lattice directions and lattice planes. Therefore, the indices are used for the discussion, investigation, and specification of specific planes and directions at the surface or within the bulk of the crystal. The direction is specified by three integers, h, k, and l and represented as [h k l]. [h k l] indicates a vector direction normal to surface of a particular plane in the cubic lattice system. The details of Miller Indices h, k, l are defined in appendix.

2.2 Damage induced by ion beam irradiation

When an energetic ion is implanted into a solid materials, it undergoes a series of collisions with host atoms and electrons until it finally stops at specified depth. In this stopping duration, energy-loss rate of incident ions strongly depends on not only the substrate material but also the mass and energy of the ion. To distinguish the different interactional mechanisms of ions between atom and electron, the processes of energy loss are divided into two parts: (1) nuclear collisions, in which lost energy is transmitted as translator motion to a target atom as a whole, and (2) electronic collisions, in which the moving particles excite or ejects orbital electrons. For convenience of research, these two collisions are liberally represented as elastic and inelastic collisions. The energy-loss rate d*E*/dx is expressed as:

$$\frac{dE}{dx} = \left.\frac{dE}{dx}\right|_n + \left.\frac{dE}{dx}\right|_e \qquad (1)$$

where the subscripts *n* and *e* denote nuclear and electronic collisions, respectively.

2.2.1 Nuclear damage and electronic damage

Nuclear collision involves large discrete energy losses and significant angular deflection of the trajectory of the projected ions as shown in fig. 2-3. This process is responsible for the production of lattice disorder by the displacement of atoms from their original positions in lattice. The contribution of electronic collisions is smaller than that of nuclear collision per collision. Therefore, the deflection of the ion trajectory and lattice disorder induced by electronic collision are negligible. The relative importance of the two energy loss process strongly depend on changing rapidly with energy *E* and atomic number *Z* of the ions. Nuclear stopping predominates for low *E* and high *Z*, whereas electronic stopping take over for high *E* and low *Z*. Electron-volt per nanometer (eV/nm) or kilo-electron-volt per micrometer (kV/μm) are used as unit of the energy loss rate. In this research, nuclear collisions are dominant compared with electronic collisions under the condition of Kr(Z=36) and E = 240 keV.

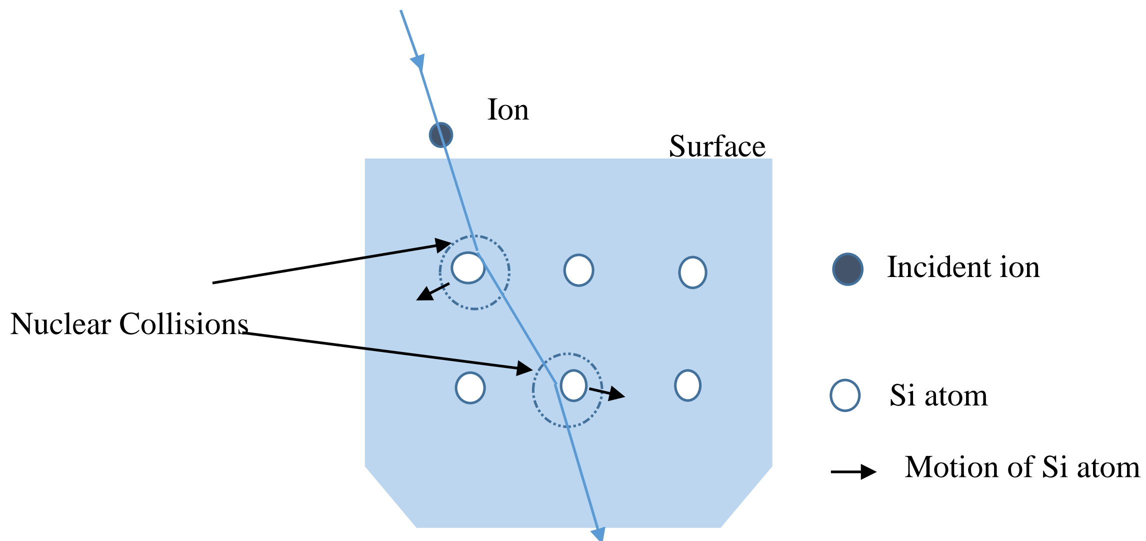

Figure 2-3 Nuclear collisions of incident ion in Si-crystal.

2.3 Modification of surface profile

Ion-beam technology, as a powerful tools, can be used to modify the surface profiles of material by introducing the expansion effect. This technology is convenient and easily to control the morphology of materials by controlling the irradiation parameters of energy and fluence. For example, the swelling height and lateral size can be controlled by ion-beam irradiation.

2.3.1 Control of the swelling height

Previous research have confirmed the swelling phenomenon can be controlled by different irradiation fluence. Zhang *et al.* [32] confirmed the swelling height can be controlled by the fluence of ion-beam on *c*-Si. Fig 2-4(a) shows an image around a border between the irradiated and un-irradiated area measured by AFM. A swelling structure can be seen clearly at irradiated area in the figure. Fig 2-4(b) shows a cross-sectional profile of the swelling

structures, measured by Alpha-step. This swelling effect are ascribed to the contribution of defect induced by ion-beam irradiation.

In addition, Trautmann *et al*. [33] confirmed the swelling of insulators induced by swift heavy ions and results are exhibited in Fig. 2-5 and Fig. 2-6.

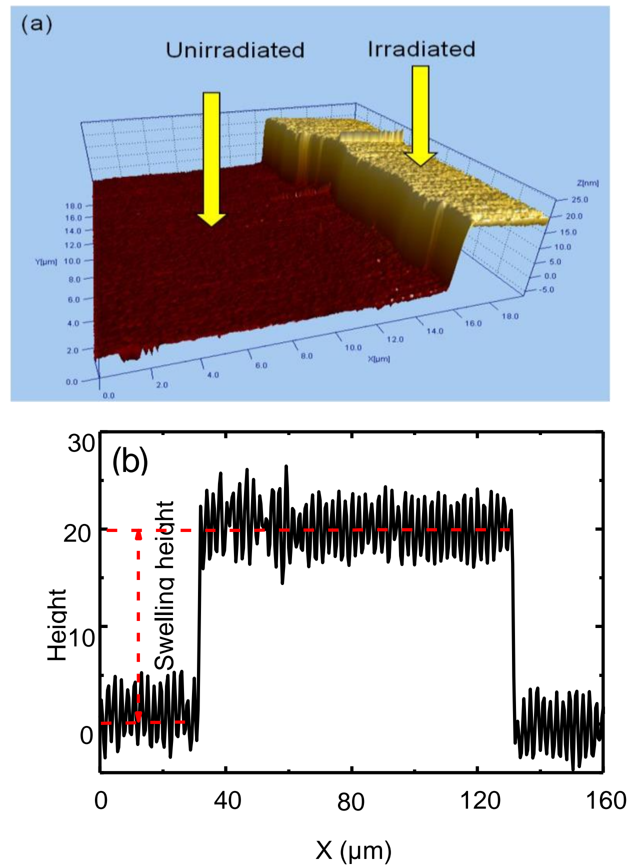

Figure 2-4. Swelling structure on Si crystal produced by expansion effect, (a) is a surface profile observed by AFM and (b) is a cross sectional profile of swelling observed by Alpha-step. The structure was fabricated by irradiating Ar^{1+} beam on Si with an energy of 90 keV and a fluence of 10^{16} /cm^2. [32]

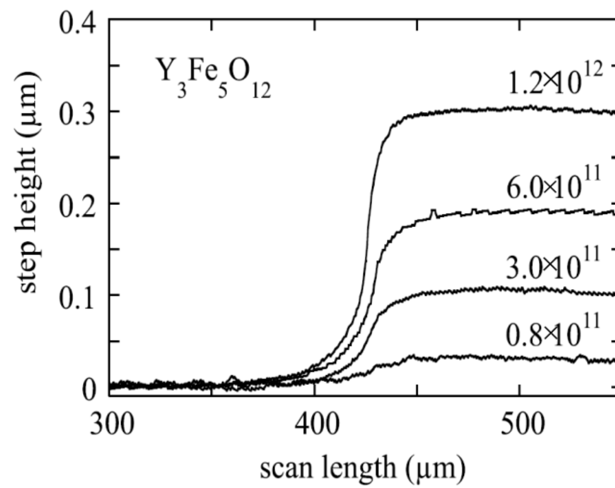

Figure 2-5 Profilometer scans for $Y_3Fe_5O_{12}$ irradiated by Pb (4 MeV/u) at different fluences (ions/cm^2) [33]

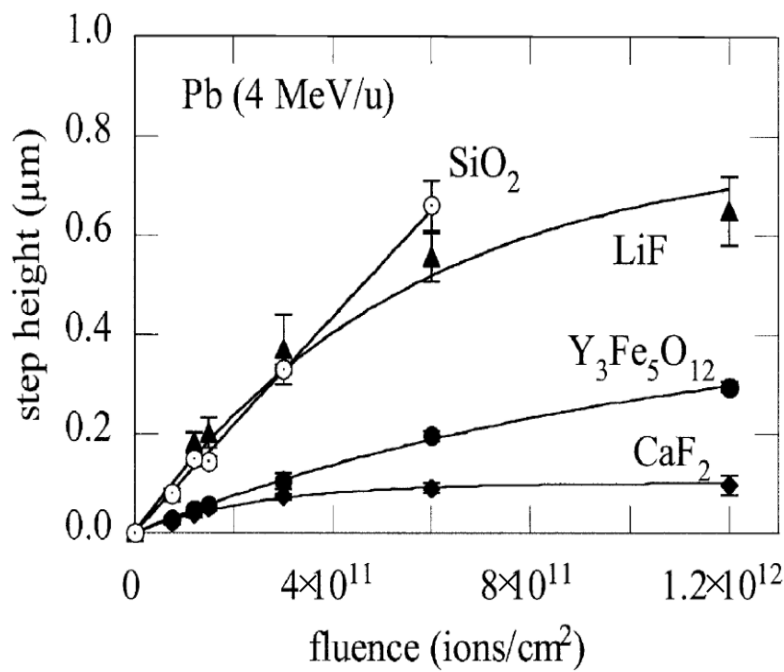

Figure 2-6 Step height versus fluence for different crystals irradiated with Pb ions of 4 MeV/u [33]

2.3.2 Control of lateral size of microstructure

To fabricate 3D structure, the control of not only the vertical size but also lateral size of structure are needed. Many researches have been performed to achieve this requirements. Ruault *et al*. [23] reported the shrinkage of nanocavities in amorphous Si under ion-beam irradiation and the results were shown in Fig. 2-7. Van Dillen *et al.* [13] reported the lateral size of silicon microstructures could be controlled by ion irradiation, as shown in Fig. 2-8. However, the material employed in these two researches was a-Si and the corresponding mechanism was plastic deformation induced by high-fluence ion beam irradiation. Therefore, the serious damage induced by ion-beam irradiation is inevitably to cause the deterioration of mechanical properties, which are one of the vital requirement for MEMS instrument. To reduce the deterioration effect, expansion effect of crystal materials induced by low-fluence ion-beam irradiation is one possible candidate.

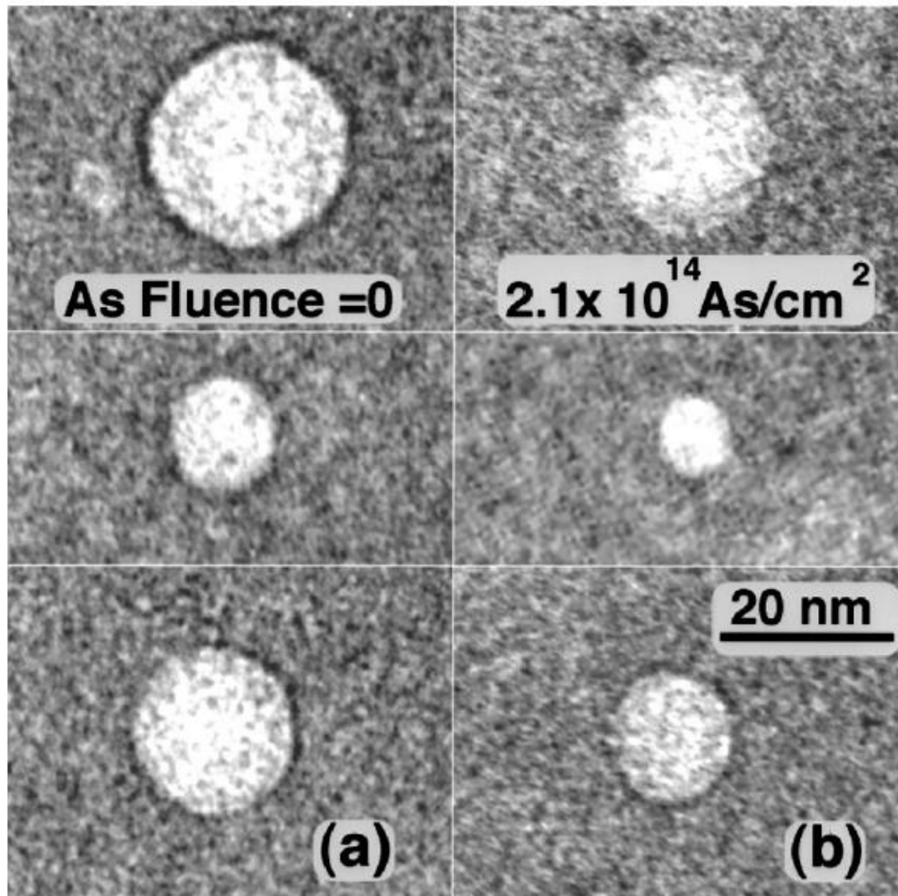

Fig. 2-7 Typical evolution of three nanocavities under As irradiation at room temperature: (a) before irradiation, and (b) after irradiation of 2.1×10^{14} As/cm^2. Irradiation at 600 K leads to similar results. [23]

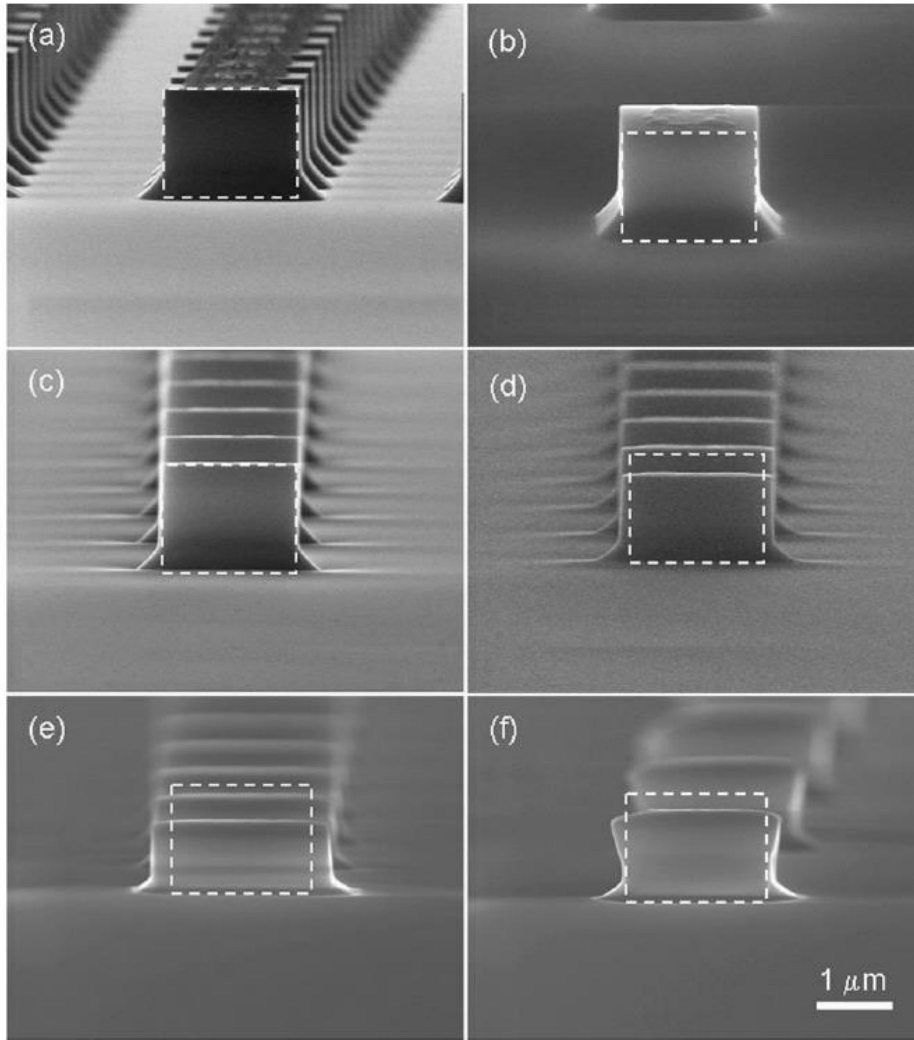

Figure 2-8 SEM images of (a) unirradiated *c*-Si(100) pillars, (b) Si pillars amorphized with 3 MeV Xe, 1.0×10^{15} cm^2, (c) *c*-Si pillars irradiated with 30 MeV Cu, 1.8×10^{15} cm^2, (d) a-Si pillars irradiated with 30 MeV Cu, 1.8×10^{15} cm^2, (e) a-Si pillars irradiated with 30MeV Cu, 8.2×10^{15} cm^2, and (f) partially amorphized Si pillars, subsequently irradiated with 30 MeV Cu, 6.1×10^{15} cm^2. SEM images were taken with a side-view. Magnification is the same for all micrographs. [13]

2.4 Mechanical properties of crystalline material

2.4.1 Anisotropic mechanical properties of c-Si

Deformation of crystalline materials under the ion beam irradiation indicate that inner stress

has been formed in the materials during the process of ion beam irradiation. The deformational degree strongly depends on the material's mechanical properties and the macroscopic hardness is generally characterized by strong intermolecular bonds. Therefore, atom's distribution in different crystalline plane strongly affect the mechanical properties of

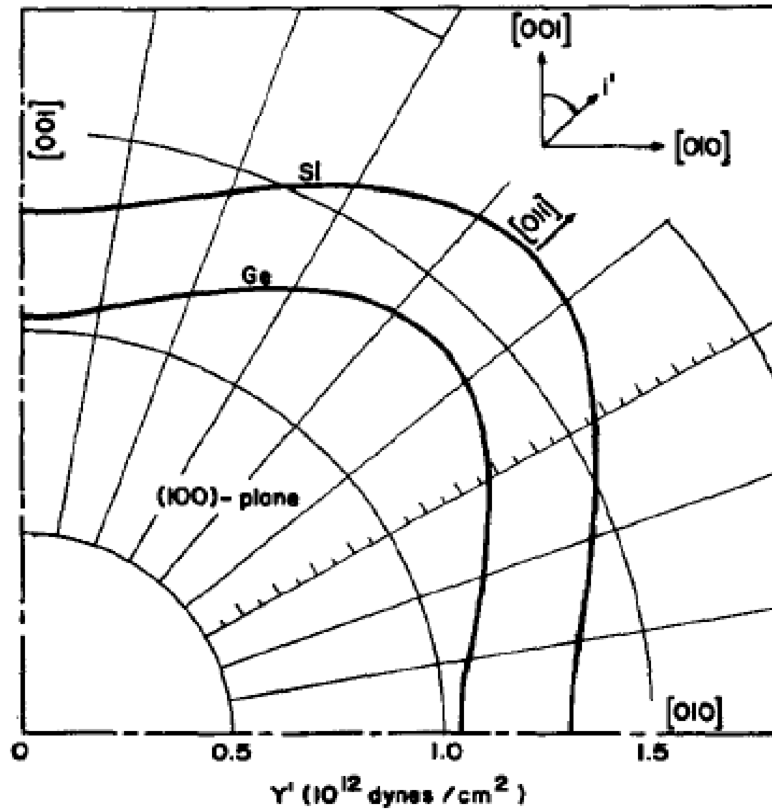

Fig. 2-9 Young's modulus of *c*-Si as a function of direction in the (100) plane [34]

crystalline materials. The anisotropic mechanical properties of crystalline silicon is expected and can affect the expansion effect in different way according to direction under the ion beam irradiation.Calculated results [34, 35] indicate that young's modulus of crystalline Si is of anisotropic properties, as shown in Fig. 2-9 and Fig. 2-10. This results implies that different deformation effect along different direction is expected in the same crystalline plane.

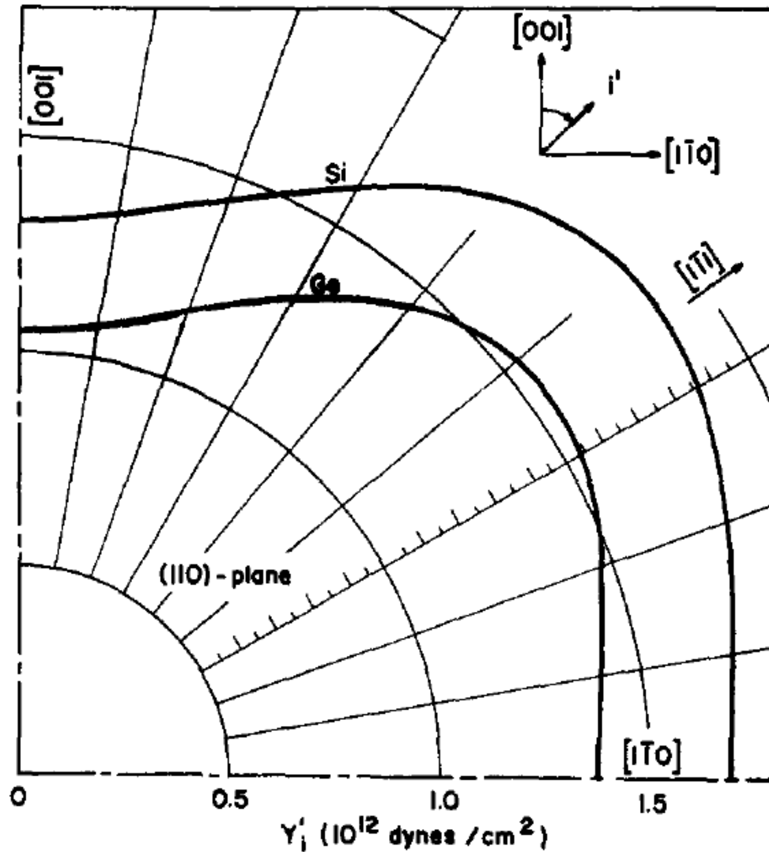

Fig. 2-10 Young's modulus of *c*-Si as a function of direction in the (110) plane [34]

2.4.2 Modification of mechanical properties

Mechanical properties are the vital requirement for MEMS instrument. Fabricating the 3D nanostructure with ion-beam technology is inevitable to result in the deterioration of mechanical properties. Therefore, to evaluate the irradiation effect on mechanical properties is quite necessary for the application of ion-beam technique. To understand the contribution of ion-beam irradiation on mechanical properties, many researches have been done. Concerning Young's modulus, The network of amorphous silicon was reported to be short and medium range order [35]. Pantchev *et al.* [36] reported the decrease in Young's modulus was associated with the structure change in the irradiated *a*-Si, such as the irradiation induced the increase in the Si-Si bond angle deviation. The structural disorder induced in the silicon network, which were associated to the variation of the short and intermediate range order, leads to a significant decrease in the mechanical stress [37]. The contribution

of irradiation effect on the decay in Young's modulus was ascribed to the induced increase in the short-range order of the silicon network. The reduction of Young's modulus for ion-beam irradiated *a*-Si could be related to the irradiation induced an increase in the Si-Si bond angel deviations [15].

Concerning nanohardness, G. Pfanner *et al*. [38] reported dangling bond defect in *a*-Si, which correspond to a network defect, was generated at suitable geometric distortions in the network while the dangling bond in crystalline silicon is usually related to the presence of a vacancy. According to ref. [15], the decrease in hardness induced by ion implantation was related to the increase in density of dangling bond, caused by atom displacements in the target. Therefore, a high concentration of defects, such as vacancies, in *c*-Si results in the decrease in long-range order of Si network to form a continuous amorphous layer, and a great number of dangling bonds were generated. According to ref. [39, 40], the density of dangling bond was about 10^{19}–10^{20} cm^{-3} in the hydrogen-free *a*-Si. Relatively lower concentration of defects was not enough to form a continuous amorphous layer but the defects still generated a good many of dangling bonds, whose density was relatively lower than that in the amorphous region.

Mechanical properties of thin layer at surface are usually measured by means of nanoindentation method. Previous researches [41, 42] indicated that the nanoindentation method induced a phase transition to cause plastic deformation via plastic flow, which is promoted by high density of dangling bond defects.

In addition, Su *et al.* [26] reported that the hardness of poly-crystalline silicon irradiated by various ions was modified by the formed bond because of the chemical effects induced by implanted ions.

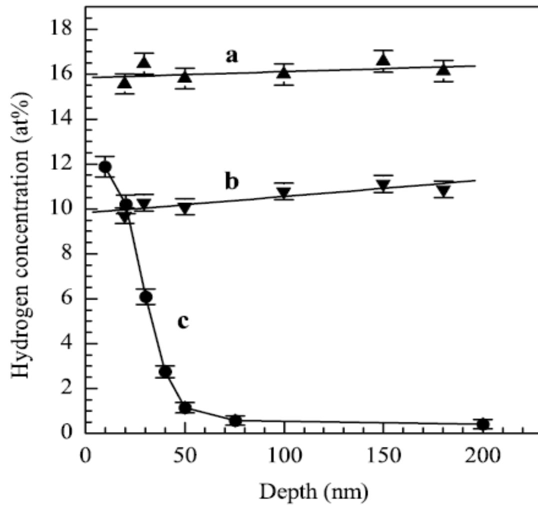

a: a-Si:H as-deposited

b: a-Si:H annealed

c: a-Si post-hydrogenated

	Depth profile	Low-depth indentation
a-Si:H as-deposited	12.30 ± 0.35	12.69 ± 0.29
a-Si:H annealed		12.03 ± 0.30
a-Si as-deposited	9.55 ± 0.35	10.15 ± 0.26
a-Si post-hydrogenated		11.27 ± 0.41

Fig. 2-11 Contribution of hydrogen concentration on the nanohardness of *a*-Si. [43]

In summary, previous researches indicated that modification of Young's modulus was ascribed to the induced decrease in the order of silicon network while modification of nanohardness was associated with dangling-bonds defects which is strongly related to the defects induced by ion-beam irradiation. Furthermore, the chemical properties can also be modified by active ions by forming bond. Fig. 2-11 show the effect on hardness.

3 Experimental method

3.1 Sample's preparation

3.1.1 Preparation of initial nanostructure on Si crystal

Czochralski-grown (Cz-Si) p-type Si <100> samples, with a size of 1.5 × 1.5 cm^2 and thickness of 0.5 mm, were used in the present studies. In order to clean and remove oxidized layer of sample surface, all of the samples were sequentially washed in acetones, ultra-pure water, 18% buffered hydrofluoric acid (BHF) and ultra-pure water. The initial patterns of stripe and nano holes on cleaned c-Si surface were fabricated by use of focused ion beam (FIB) machine (FEI QUANTA 3D 200i dual beam system). A length and a height of the stripe are 10 μm and ~500 nm, respectively. Stripes with four different widths, about 200, 300, 400 nm, and 500 nm, were prepared. A depth and a diameter of nano hole is ~500 nm

and ~500 nm, respectively.

According to ref. [44], damaged layer is produced on the surface of nanostructure by Ga-ion beam irradiation in the process of initial-structure (FIB) fabrication. In order to remove the layer, processed samples were etched with 18% BHF for 12 minutes under the condition of ultrasonic at RT. The residual damages, such as point defect, were expected to remain in etched sample. In order to remove such residual damages, we performed annealing process in an argon ambient environment at atmospheric pressure with desktop lamp heating ULAVC-MILA-3000. The condition of annealing process described in ref. [45] was applied. The preparation procedures of initial structure are shown in Fig. 3-1.

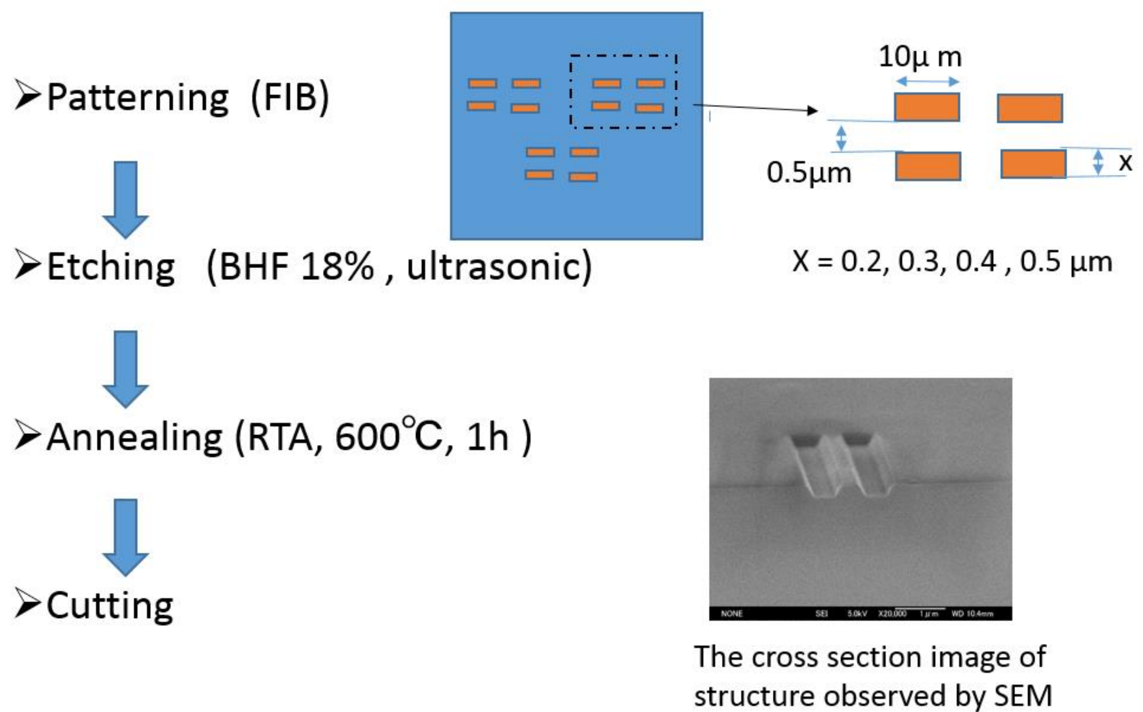

Fig. 3-1 Procedure to prepare initial structure on crystal Si.

3.1.2 Preparation of sample for nanoindentations test

Czochralski-grown (Cz-Si) p-type Si <100> samples, with a size of 1.5 × 1.5 cm^2 and thickness of 0.5 mm, were used in the present studies. In order to clean and remove oxidized

layer of sample surface, all of the samples were sequentially washed in acetones, ultra-pure water, 18% buffered hydrofluoric acid (BHF) and ultra-pure water.

3.2 Irradiation of samples by Kr-ion irradiation

3.2.1 Condition of irradiation

In order to induce the lateral deformation in initial structures, which were prepared in the above process, Kr^{+2} beams with energy of 240 keV was implanted at a direction titled about 5° away from the normal to avoid channeling in the *c*-Si nanostructures. Kr beam was prepared by a 10-GHz NANOGAN, which is an ECR ion source installed at Kochi University of Technology [46]. The initial structures were irradiated with the fluence of 6, 8, 10, 30, and 50 x 10^{13} ions/cm^2. For modification of mechanical properties, the sample were irradiated with the fluence of 1 and 5 x 10^{14} ions/cm^2.

3.2.2 Selection of charge state

Fig. 3-2 is the schematic of ion beam irradiation system. Part 1 is the ion source, which generated the Kr-ion. Part 2 is analyzing system for selection of element and charge state by an electromagnet. Part 3 is the irradiation system, where c-Si samples were irradiated.

The charge state was confirmed by mass spectroscopy measured, as shown in Fig. 3-3. The current applied to electromagnet is evaluated by

$$I = \frac{\sqrt{2MU/ne}}{\alpha R} \quad , \qquad (1)$$

where, *I* is current of magnetic corresponding to charge state; *M* is atomic mass of ion; *U* is acceleration voltage; *n* is the charge state of ions; *R* is radius of electromagnetics, 0.25 m; *α* is constant, 0.025. therefore, we can get the corresponding current for ions with objective charge state to select the charge state.

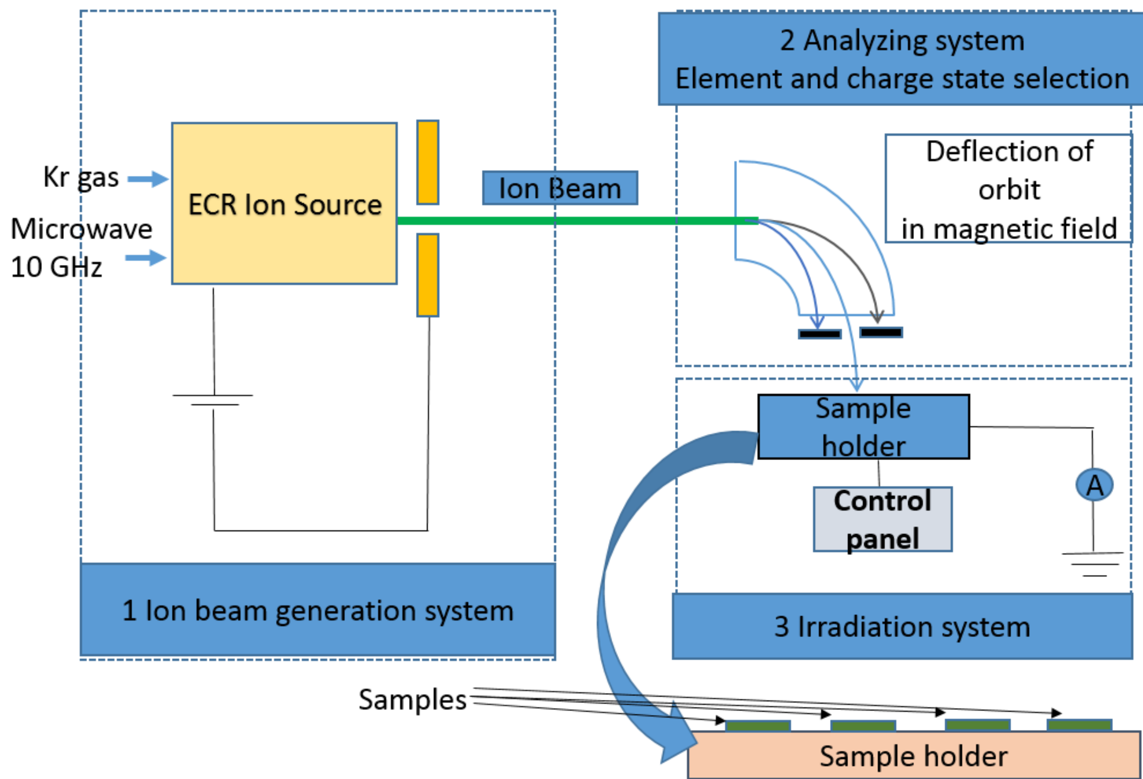

Fig. 3-2 Schematic picture of ion-beam irradiation system. *c*-Si samples are mounted on a sample holder.

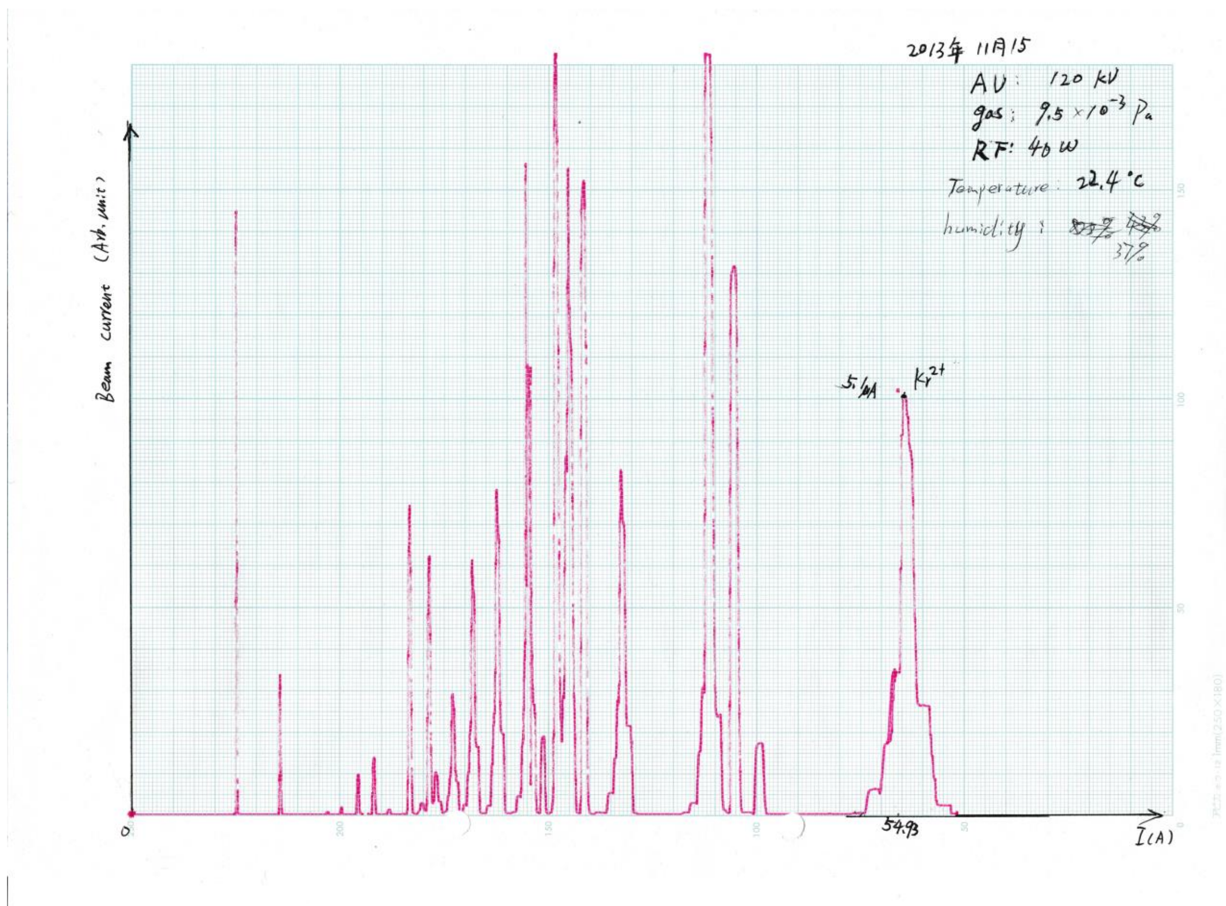

Fig. 3-3 Typical mass spectrum. The horizontal axis indicates current applied to the analyzing magnet. Kr^{2+} indicated in the figure.

3.2.3 Measurement of fluence

The fluence is important parameter in the process of ion-beam irradiation. It is evaluated by the formula:

$$F = \frac{i \times t}{n \times e} \quad , \qquad (3)$$

where, *F* is fluence; *i* is target current, which can be directly measured in the experimental process; *t* is the irradiation time; *n* is the charge state of ion and e is the elementary charge.

3.3 Evaluation of irradiation effect

In order to observe the size of nanostructures along the lateral direction, the cross-section was prepared by a cutting to cross the stripe pattern vertically. Cross sectional profiles of nanostructure were measured by field emission scanning electron microscopy (FE-SEM, JEOL, JSM-7401F) before and after irradiation.

As described in the previous section, the growing features of amorphization corresponding to irradiation effect is important information to understand the mechanism of lateral deformation induced by low fluence ion beam irradiation. In order to obtain information on amorphization induced by low fluence ion beam irradiation in nanostructures, Raman spectrometer (HR 800 Horiba, 532 nm of laser) and transmission electron microscopy (TEM, JEOL 2100F) were applied to evaluate the effect of ion beam irradiation. Observed Raman spectrum and TEM images would provide amorphous fraction and thickness of amorphous layer, respectively. RBS-C method was utilized to provide the defect distribution and the thickness of amorphous layer in Si target.

3.3.1 Raman spectroscopy

The scattering occurs when a beam of monochromatic light passes through a crystal, and the scattering involves Rayleigh and Raman scattering, as shown in Fig. 3-4. When the monochromatic laser light with frequency υ_0 excites the sample, there are three cases to be induced. 1) The molecule absorbs a photon with υ_0 to reach an excited state. Then, the excited molecule returns back to the ground state emitting light with same frequency υ_0. This process is named Rayleigh scattering. The Rayleigh scattering is induced by an elastic collision between the incident photons and the phonons in materials, thus generates light with the same vibrations frequency as the incident ray. 2) The molecule absorbs a photon υ_0, part of the photon energy is transferred to Raman-active mode with frequency υ_1. The final frequency of the scattered light is $\upsilon_0 - \upsilon_1$. It is named Stokes Raman scattering. The Raman scattering is induced by the inelastic collision between incident photons and phonons in the

materials, hence produce the incident photons with different vibration frequency. 3) The molecule absorbs a photon υ_0, part of the photon energy is transferred to Raman-active mode with frequency υ_1. The final frequency of the scattered light is $\upsilon_0 + \upsilon_1$. It is named Anti - Stokes Raman scattering. The intensity of Rayleigh scattering is about 10^{-3} of the incident light and the Raman scattering is about the 10^{-3} of the Rayleigh scattering. Raman scattering is typically very weak, and as a result the main difficulty of Raman spectroscopy is separating the weak inelastically scattered light from the intense Rayleigh scattered laser light.

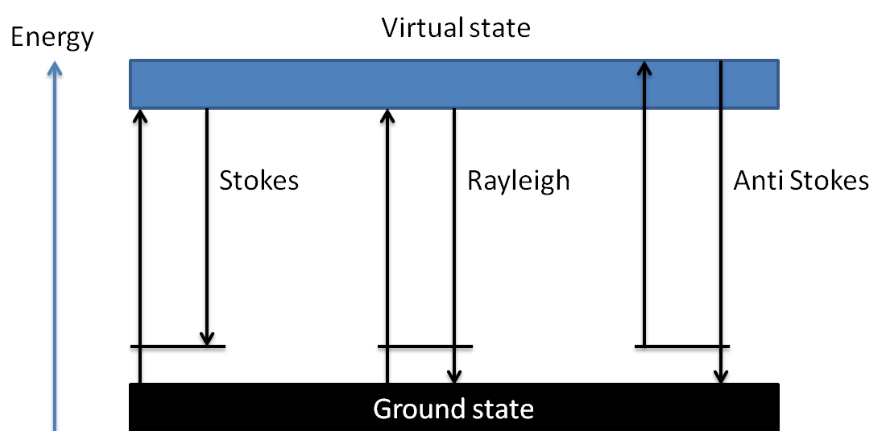

Fig. 3-4. Energy level diagram to show the states involved in Raman signal. The line thickness is roughly proportional to the signal strength from the different transitions.

The Raman shift is strongly influenced by microscopic structure, impurity and residual strains, which lead to changes in phonon frequencies - shift of peaks, broadening of Raman peaks, and breakdown of Raman selection rules. Laser Raman spectroscopy can detect the amorphous silicon as well as residual stress in silicon wafer.

There are a number of advanced types of Raman spectroscopy, such as surface-enhanced Raman, polarised Raman, tip-enhanced Raman, resonance Raman, transmission Raman, stimulated Raman (analogous to stimulated emission), spatially offset Raman, and hyper Raman.

In this study, Raman spectroscopy was applied to characterize crystalline to amorphous phase transition of *c*-Si induced by ion beam irradiation. Raman spectra were measured at

RT under the backscattering geometry using the 532 nm of laser (HR 800 Horiba).

3.3.2 Scanning electron microscopy measurement

Scanning electron microscopy (SEM) is a powerful method to evaluate the 2-dimensional surface morphology. The surface morphologies were observed by FE-SEM system, operating at 5 kV, was used to measure the surface of samples. SEM consists of 1) electron optical system, 2) signal receiving system, 3) power supply system and 4) vacuum system. The working principle of SEM is shown in Fig. 3-5.

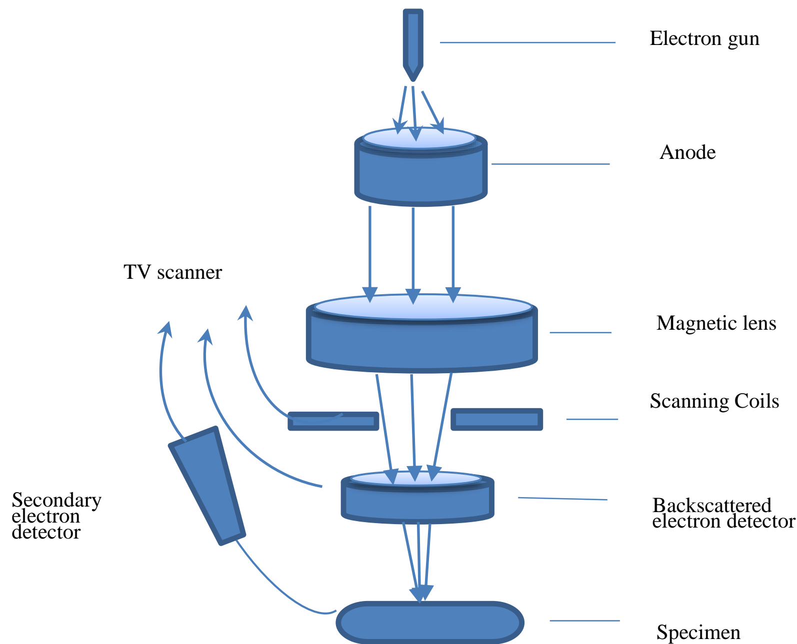

Fig. 3-5. Working principle of SEM

3.3.3 Transmission Electron Microscope

The transmission electron microscope (TEM) operates on the same basic principles as the optical microscope, except for the uses of electrons instead of light. What you can see with a light microscope is limited by the wavelength of light. TEMs use electrons as "light source" and their much shorter wavelength make a great possibility to achieve much better get a resolution a thousand times better than with an optical microscope. The basic working principle is shown in Fig. 3-6.

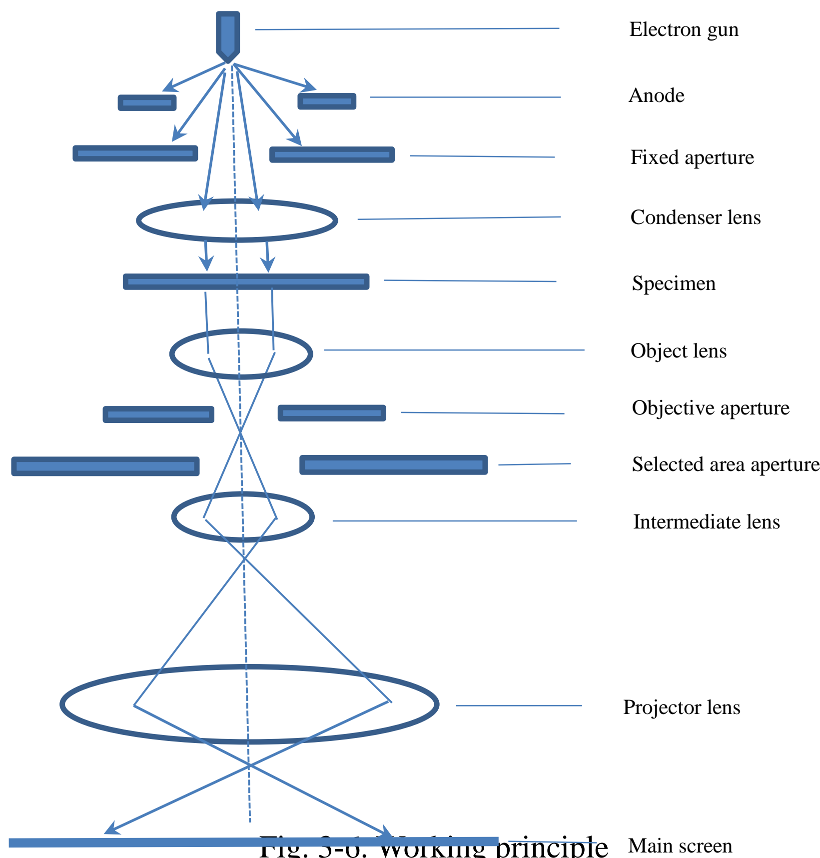

Fig. 3-6. Working principle

An electron gun at the top of the microscope emits the electrons that travel through vacuum in the column of the microscope. Instead of glass lenses focusing the light in the light microscope, the TEM uses electromagnetic lenses to focus the electrons into a very thin beam. The electron beam then travels through the specimen to be evaluated. Depending on the density of the material present, some of the electrons are scattered and disappear from the beam. At the bottom of the microscope, the unscattered electrons hit a fluorescent screen, which gives rise to an image of the specimen with its different parts displayed in varied darkness according to their density. The image can be observed directly by the operator or photographed with a camera.

In TEM, an acceleration energy of several hundred keV is utilized to illuminate the samples, which thickness is typically ～100 nm. There are two fundamental imaging models TEM: diffraction and image model.

In the diffraction mode, normally the objective aperture is opened wide and the selected-area aperture is inserted to select the area of interest, here comes the term selected-area electron diffraction (SAED). In the image mode, the selected area diffraction (SAD) aperture is usually opened wide and the objective aperture is inserted to select interested spots.

Bright field (BF) and dark field (DF) regimes are usually utilized to take photos of samples. In the BF regime, the objective aperture is adjusted so that it does not intercept the transmitted spot. Several diffracted spots around the transmitted spot can be selected also. However, it is a trade-off between the brightness and contrast, the more selected spots make the image brighter, and male the image worse contrast. To take a simple DF images, the objective aperture is adjusted so that it intercepts the transmitted spot. As a result, merely diffracted spots are selected. DF images taken in this way are generally not preferable because the diffracted beams travel off from the optic axis, which increases aberration and astigmatism.

High-resolution TEM is one of imaging modes of TEMs that allows the imaging of the crystallographic structure of a sample at an atomic scale. HRTEM images result from phase-contrast. When electron waves travel across very thin sample (typically less than 50 nm), as the result of scattering by the sample's atoms, the electron waves which pass through the sample, do not change with uniform amplitude, but obtain phase shift.

In this study, the microstructural evolutions of the Kr-irradiated *c*-Si target was studied by cross-sectional TEMs operating at an accelerating voltage of 200 kV. Structural changes associated with ion irradiation were observed by bright-field images (BFIs) and HRTEM. The samples were prepared by focus ion beam (FIB) - FEI QUANTA 3D 200i operating at an accelerating voltage of 30 kV and the ion species is Ga. Pt atoms were deposited on the sample surface to form a protection layer. The Si sample was cut into a small piece of sample, and was placed on a copper holder with three convex protrusions. Finally, prepared piece was milled to thickness of ～100 nm by mean of the focused Ga beam.

3.3.4 Nanoindentation

Nanoindentation method is a widely used in the characterization of small-scale mechanical behavior, such as elastic modulus and hardness. Since its original development, the method has undergone numerous refinements and changes brought about by improvements to testing equipment and techniques as well as from advances in our understanding of the mechanics of elastic–plastic contact. Here, the basic principle will be just introduced briefly.

A schematic representation of a typical data set obtained with a Berkovich indenter is presented in Fig. 3-7, where the parameter P designates the load and h the displacement relative to the initial undeformed surface. For modeling purposes, deformation during loading is assumed to be both elastic and plastic in nature as the permanent hardness impression forms. During unloading, it is assumed that only the elastic displacements are recovered; it is the elastic nature of the unloading curve that facilitates the analysis. For this reason, the method does not apply to materials in which plasticity reverses during unloading.

There are three important quantities that must be measured from the P–h curves: the maximum load, P_{max}, the maximum displacement, h_{max}, and the elastic unloading stiffness, $S = dP/dh$, defined as the slope of the upper portion of the unloading curve during the initial stages of unloading (also called the contact stiffness). The accuracy of hardness and modulus measurement depends inherently on how well these parameters can be measured experimentally. Another important quantity is the final depth, h_f, the permanent depth of penetration after the indenter is fully unloaded.

Experiments have shown that unloading curves are distinctly curved and usually well approximated by the power law relation:

$$P = \alpha(h - h_f)^m, \qquad (1)$$

Where α and m are power law fitting constants.

The exact procedure used to measure H and E is based on the unloading processes. The procedure is shown schematically in Fig. 3-8, in which it is assumed that the behavior of the Berkovich indenter can be modeled by a conical indenter with a half-included angle, Φ, that

gives the same depth-to- area relationship, Φ=70.3°. The basic assumption is that the contact periphery sinks in a manner that can be described by models for indentation of a flat elastic half-space by rigid punches of simple geometry. This assumption limits the applicability of the method because it does not account for the pile-up of material at the contact periphery that occurs in some elastic–plastic materials. Assuming, however, that pile-up is negligible, the elastic models show that the amount of sink-in, h_s, is given by:

$$h_s = {\varepsilon P_{max}}/{S} \quad , \quad (2)$$

where ε is a constant that depends on the geometry of the indenter. Important values are: ε = 0.72 for a conical punch, ε = 0.75 for a paraboloid of revolution, and ε =1.00 for a flat punch.

Using Eq. (2) to approximate the vertical displacement of the contact periphery, it follows from the geometry of Fig. 3-8 that the depth along which contact is made between the indenter and the specimen,$h_c = h_{max} - h_c$, is:

$$h_c = h_{max} - {\varepsilon P_{max}}/{S} \quad , \quad (3)$$

Letting *F(d)* be an "area function" that describes the projected (or cross sectional) area of the indenter at a distance *d* back from its tip, the contact area *A* is then

$$A = F(h_c) \quad , \quad (4)$$

The area function, also sometimes called the indenter shape function, must carefully be calibrated by independent measurements so that deviations from nonideal indenter geometry are taken into account. These deviations can be quite severe near the tip of the Berkovich indenter, where some rounding inevitably occurs during the grinding process. Although a basic procedure for determining the area function was presented as part of the original method, Oliver *et al.* had made significant changes to it in recent years [47]. Once the contact area is determined, the hardness is estimated from:

$$H = P_{max} / A \quad , \quad (5)$$

Note that because this definition of hardness is based on the contact area under load, it may

deviate from the traditional hardness measured from the area of the residual hardness impression if there is significant elastic recovery during unloading. However, this is generally important only in materials with extremely small values of E/H.

Measurement of the elastic modulus follows from its relationship to contact area and the measured unloading stiffness through the relation

$$S = \beta \frac{2}{\sqrt{\pi}} E_{eff} \sqrt{A} \quad , \quad (6)$$

where E_{eff} is the effective elastic modulus defined by

$$\frac{1}{E_{eff}} = \frac{1-v^2}{E} + \frac{1-v_i^2}{E_i} \quad , \quad (7)$$

The effective elastic modulus takes into account the fact that elastic displacements occur in both the specimen, with Young's modulus E and Poisson's ratio v, and the indenter, with elastic constants E_i and v_i. Note that Eq. (6) is a very general relation that applies to any axisymmetric indenter. It is not limited to a specific simple geometry, even though it is often associated with flat punch indentation. Although originally derived for elastic contact only, it has subsequently been shown to apply equally well to elastic–plastic contact and that small perturbations from pure axisymmetry geometry do not effect it either. It is also unaffected by pile-up and sink-in.

The experiment conditions of our experiment are as follows: the mechanical properties, as a function of the depth, were measured by Nano Indenter XP/DCM (Agilent Technologies) equipped with a Berkovich diamond indenter. The continuous stiffness measurement (CSM) mode was employed at room temperature and the principle of continuous measurement of hardness and Young's modulus was described in ref. [48]. During the penetration, the indenter vibrates with amplitude of 2 nm at a frequency of 45 Hz. A constant strain rate of 0.05 s^{-1} was applied during loading with a 10 s hold period at peak load. Ten indentations were made in each sample with a maximum depth of 500 nm.

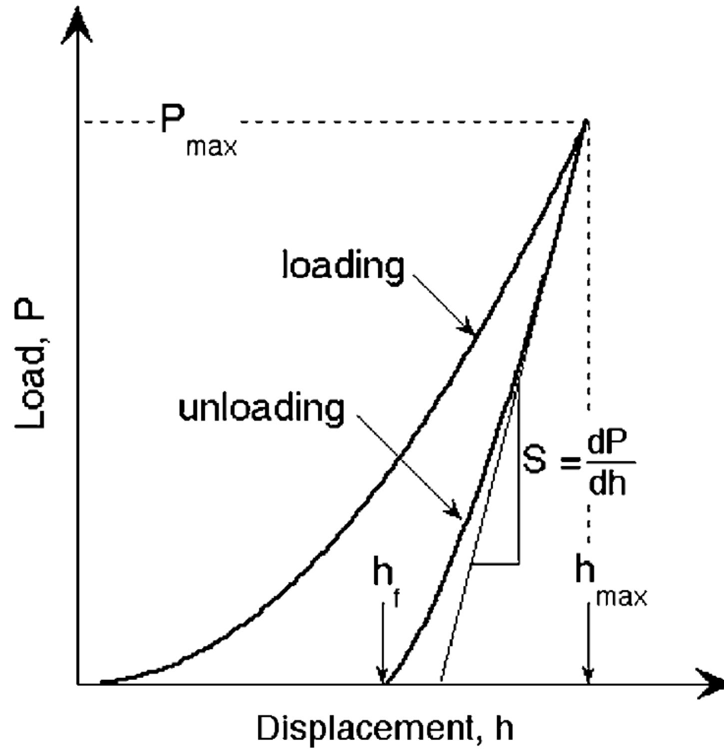

Fig. 3-7 Schematic of indentation load-displacement curve obtained in indentaion measurement. [47]

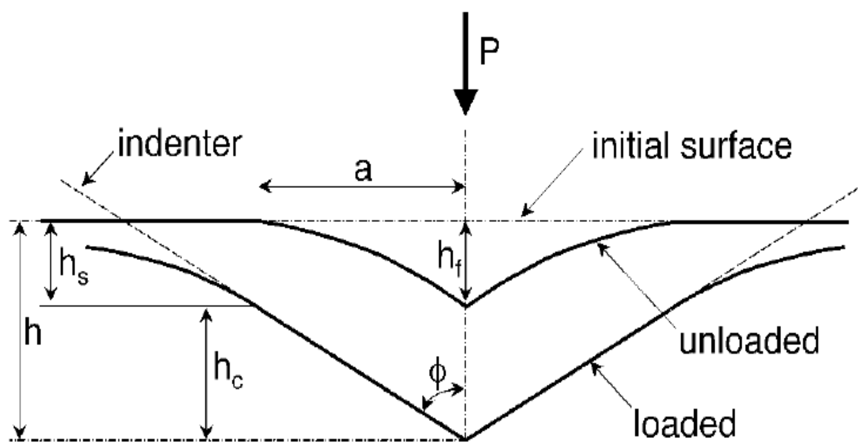

Fig. 3-8 Schematic illustration of the unloading process showing parameters charactering the contact geometry. [47]

3.3.5 Rutherford backscattering spectrometry channeling (RBS-C)

The Rutherford backscattering-channeling (RBS-C) technique has been widely employed to analyze near-surface layer of solids, elemental composition, and depth profiling of individual elements. The advantage of this technique is quantitative without reference samples and non-destructive. In this research, RBS-C technique was utilized to evaluate the depth

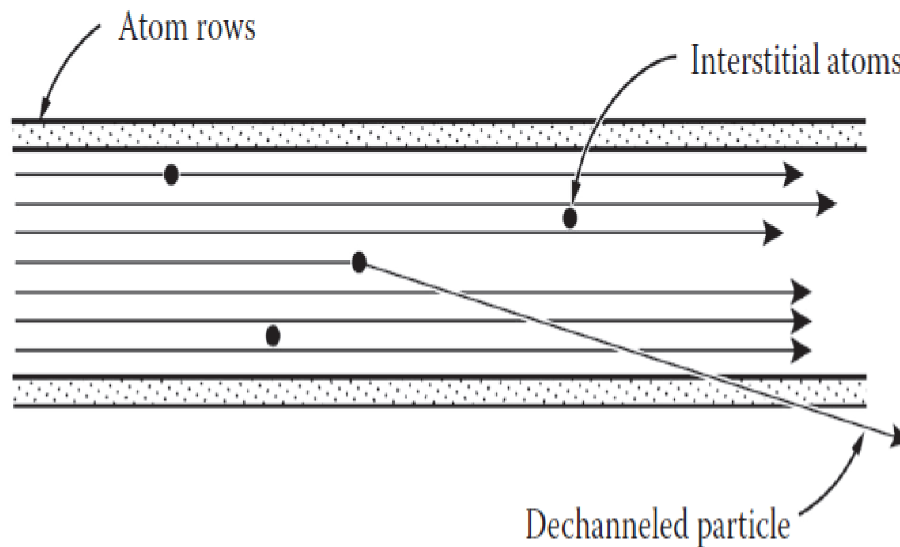

Fig. 3-9 Dechanneling effect induced by interstitial

profile of defect. Here, the principle of RBS-C is introduced. When the material is perfect crystalline, energetic ions' moving along the atom rows, can penetrate without scattering. But when there are some defects, such as interstitial atoms, the ions will be dechanneled, as shown in Fig. 3-9. The relation between ion defect and RBS spectroscopy is shown in Fig. 3-10.

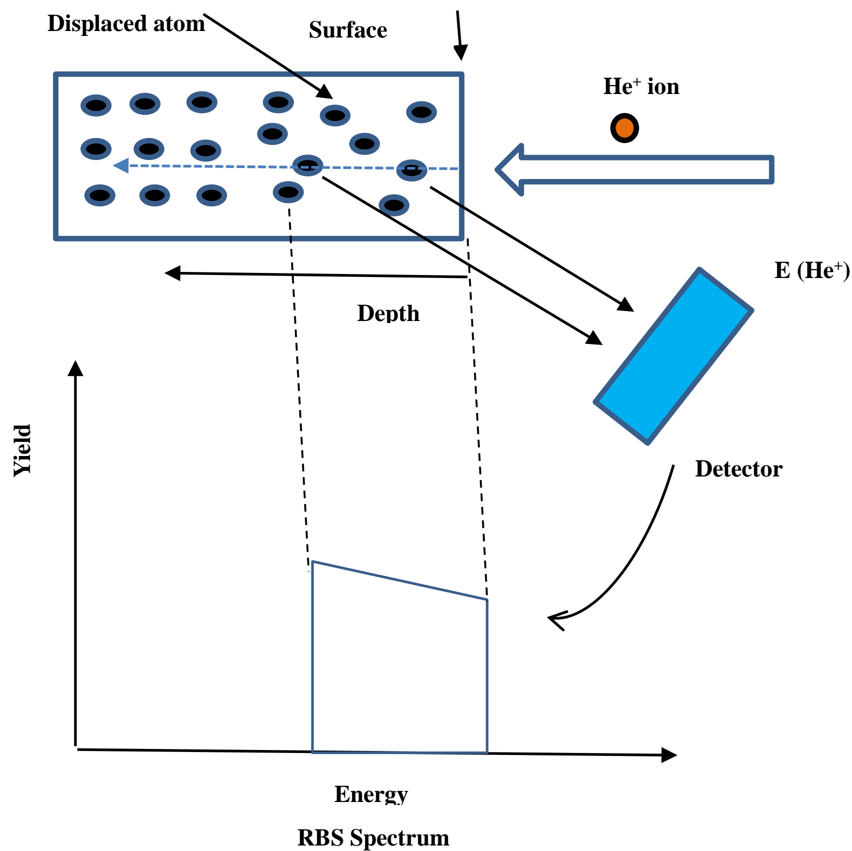

Fig. 3-10 Schematic of the relation between and defect and RBS Spectrum.

3.4 Calculation of damage distribution by SRIM

The simulation of ion beam irradiation process has been developed in several decades. The stopping and Range of Ions in Matter (SRIM), developed by James F. Ziegler, Jochen P. Biersack, and Matthias D. Ziegler since 1980s, is a popular software to calculate the irradiation effect. The software of SRIM is based on a Monte Carlo simulation method, namely the binary collision approximation with a random selection of the impact parameter of the next colliding ion. TRIM is a core component contained in programs of SRIM. SRIM can calculate the stopping and range of ions with energy of 10 eV – 2 GeV/amu into matter using a quantum mechanical treatment of ion-atom collisions. During the collisions, the ion and atoms have a screened Coulomb collision, including exchange and correlation interaction between the overlapping electron shells.

There are advantages of SRIM software: The three-dimensional distribution of the ions in

the solid and its parameters, such as penetration depth, its spread along the ion beam (called stragglling) and perpendicular to it, all target atom cascades in the target are followed in detail. We can get the value of concentration of vacancies, sputtering rate, ionization, and phonon production in the target material. The disadvantages of SRIM software: It doesn't take account of the crystalline structure dynamic composition changes by different irradiation parameters. It cannot simulate the various contribution of sample temperatures.

According to previous studies [20], expansion effect had strong relation with damages induced by ion beam implantation. In order to evaluate the implantation effect, SRIM-2008 was used in the "detailed calculation with full damage cascades" mode for 5000 projectile Kr-ion with kinetic energies 240 keV [49]. Calculated distributions of vacancies and ions are showed in Fig. 3-11 and Fig. 3-12, respectively. This calculation does not consider the self-annealing effect and the nonlinear effect, such as interaction between defects.

The distribution of vacancy, induced by the implantation of 240 keV Kr-beam, is close to Gaussian distribution. Vacancies distribution covers the depth range from 0 nm to 300 nm and shows its maximum at the depth of about 100 nm. As shown in Fig. 3-12, concentration distribution of Kr-ion also shows Gaussian-like distribution, which is characterized by projection range, 142.6 nm, and struggling, 44.9 nm. Considering calculated distribution, major part of Kr-ions, ~75%, stops at the depth between 100 nm and 190 nm. According to the contributions of vacancies and impurities (Kr) to the damage of Si, the region of interests was focused in the range of depth from 0 nm to 200.

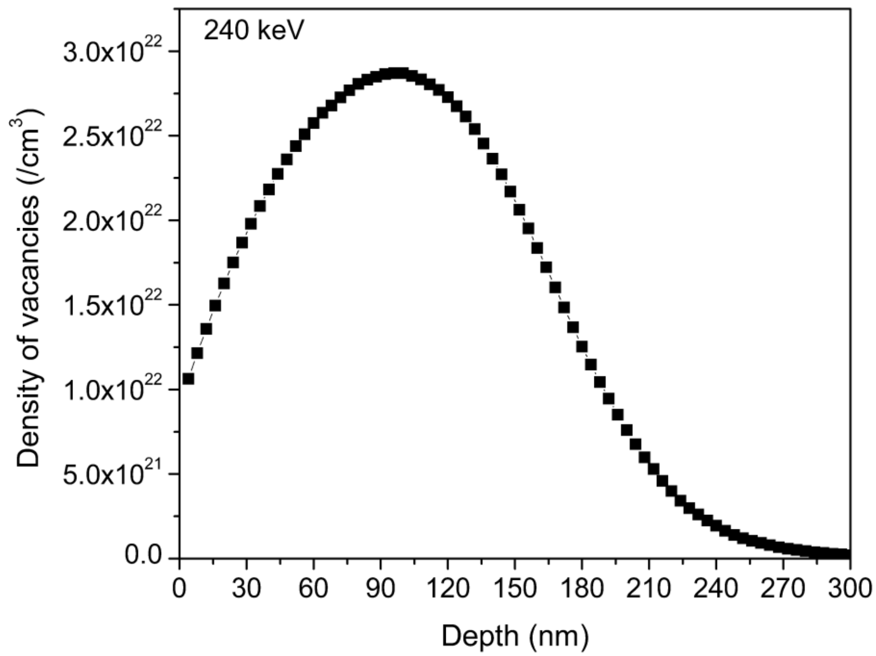

FIG. 3-11 Density distribution of vacancy in *c*-Si induced by 240 keV Kr-beam calculated by SRIM

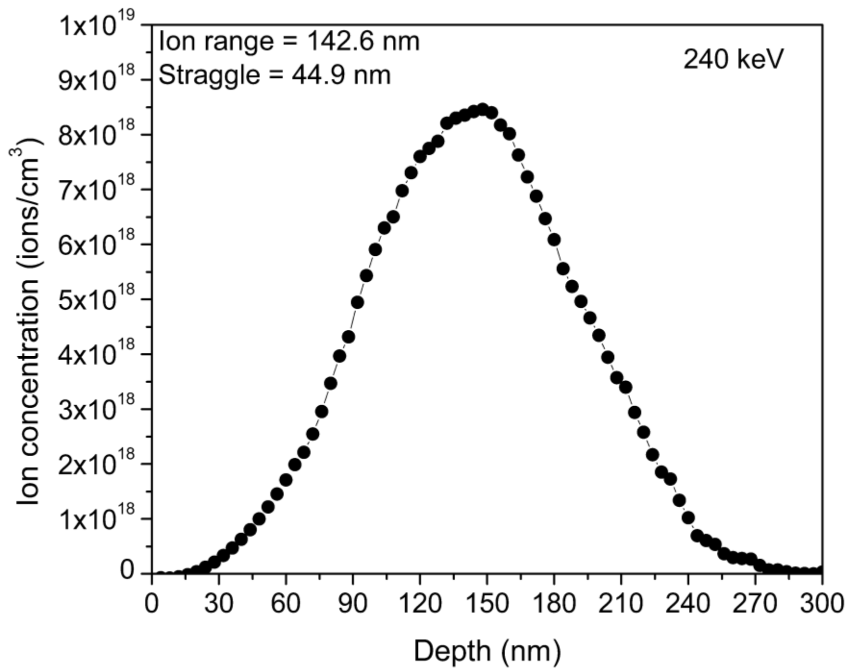

FIG. 3-12 Ion distribution in c-Si induced by 240 keV Kr-ion calculated by SRIM

4 Modification of morphologies of c-Si nanostructure

4.1 Observation of stripe structures and nano-hole structure by SEM

Typical SEM images of stripe structures before and after Kr-beam irradiation are shown in Fig. 4-1. Fig. 4-1(a) shows the cross section of a center pile in stripe structure at a given cutting plane before Kr-beam irradiation. The slope of sidewalls and curvature at the top edges were found in the observed cross sections. Therefore, the present study is on the deformation of stripe structure with a taper-shaped cross section. It is considered that those features arise from preparation processes of the initial structure. The cross section of the stripe structure after Kr-beam irradiation is shown in Fig. 4-1(b) and the remarkable lateral deformation is identified as an increase in the width of a center pile, compared with Fig. 4-1(a). Concerning the nano-hole structure, the remarkable shrinkage in the diameter is identified, as shown in Fig. 4-2.

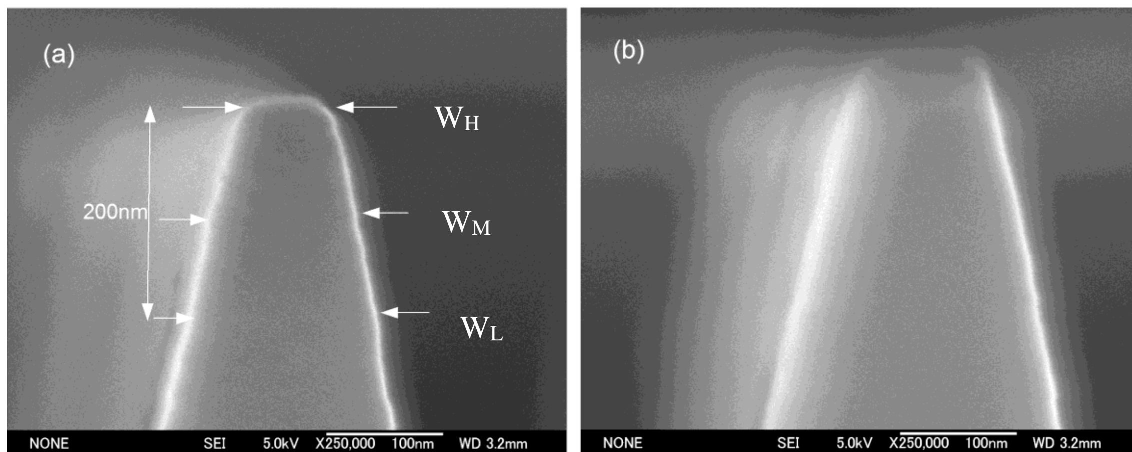

FIG. 4-1 SEM images of the stripe structure. (a) and (b) show cross sections of the center piles in stripe structures before and after the irradiation of Kr beams with 240 keV, 8×10^{13} ions/cm^2.

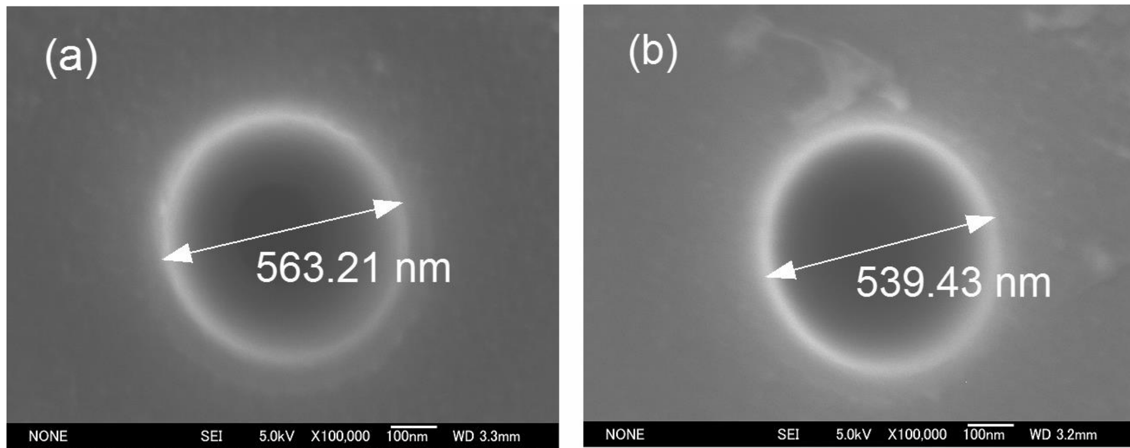

FIG. 4-2 SEM images of nano-hole structure. (a) and (b) show top views of the nano-hole structure before and after the irradiation of Kr beams with 240 keV , 1 x 10^{14} ions/cm^2.

4.1.1 Lateral deformation of nanostructures irradiated by Kr-beam

4.1.1.1 Definition of change in lateral size for stripe/nano-hole structure

The widths of the center piles in stripe structures were measured at three different levels: higher (W_H), middle (W_M) and lower (W_L) positions, which are defined in Fig. 4-1(a) according to consideration of the SRIM calculation in section 3.4. Because of a curvature at the top edge, relatively large ambiguities were observed in W_H. Therefore, the widths W_M and W_L are used in the following discussion. As the central value, the average of W_M and W_L is employed. The width change of stripe structure was defined by the formula: width change = $W_{after} – W_{before}$.

The diameter of nano-hole structure was measured based on the top view of SEM observation and the diameter change was defined by the formula:

diameter change = D_{before} - D_{after}.

4.1.2 Lateral deformation as a function of fluence

Fig. 4-3 and Fig. 4-4 indicate that the remarkable fluence dependence of the behavior of the

lateral deformation for stripe and nano-hole structures, respectively. For both structures, in the case of the same irradiation energy (240 keV), the lateral deformation of nano-structure firstly increase and then decrease with irradiation fluence. For the stipe structure with a width of 100 ~ 200 nm, the relation between the width change and the fluence of Kr-beam is shown in Fig. 4-3. The width change, which is provided from one sample, is shown with no error bars. As shown in Fig. 4-3, the remarkable fluence dependence of the lateral deformation was observed for stripe structures. The width change increases up to a fluence of 8 x 10^{13} ions/cm^2, and decreases to almost zero at a fluence of 5 x 10^{14} ions/cm^2. For nano-hole structure, the shrinkage of diameter is observed as shown in Fig. 4-4. The figure shows that the shrinkage increases gradually up to the fluence of 3 x 10 ^{14}/cm^2, and then turn to decrease steeply with fluence. Although there is difference in critical fluence, which corresponds to the maximum of lateral deformation, the general tendency is almost same for width change of stripe structure and diameter change of nano-hole.

To avoid any contribution of ambiguity in the initial structure size induced by the etching process, the lateral expansion rate was calculated, as shown in Fig. 4-5. Since sidewalls of a center pile have a slope with a tilt angle of 70 ~ 80 degree, densities of implanted ions and defects changes along a lateral direction even at same level. This effect would relax the intrinsic level dependence and gives obvious contribution for structures with small width. Therefore, the expansion rates obtained for W_M and W_L are averaged and the error bars are defined by those differences. Calculated lateral expansion rate shows similar behavior with the width change, and becomes maximum value of 30% with a fluence of 8 ~ 10 x 10^{13} ions/cm^2.

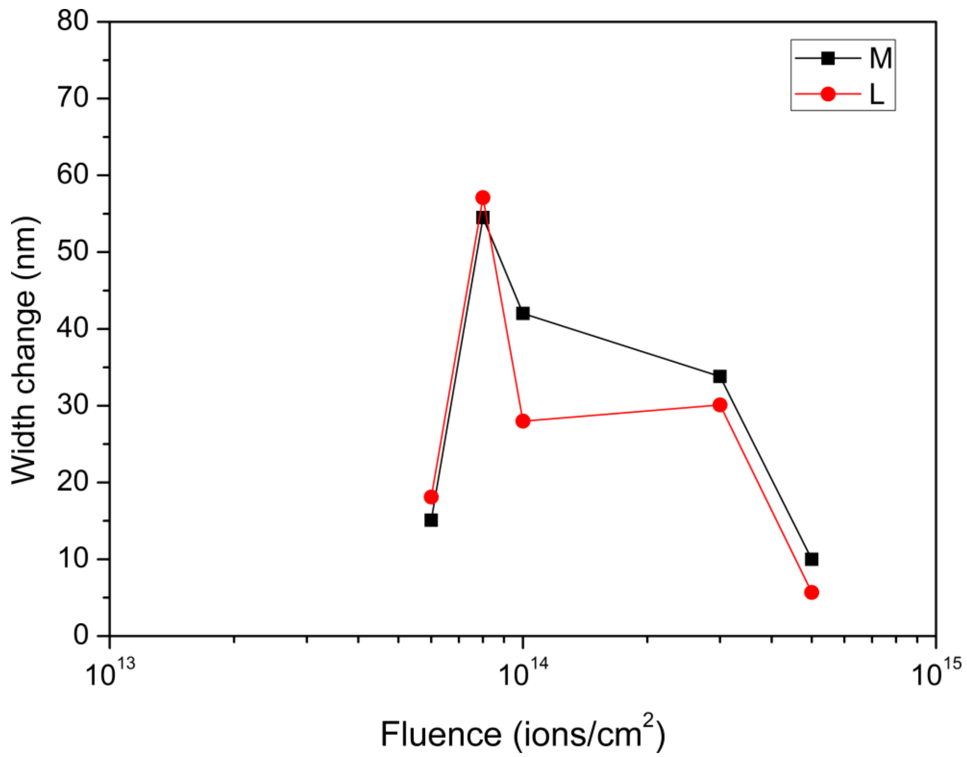

FIG. 4-3 Fluence dependence of width change in the center pile of the stripe structure for lateral size of 100 nm ~ 200 nm.

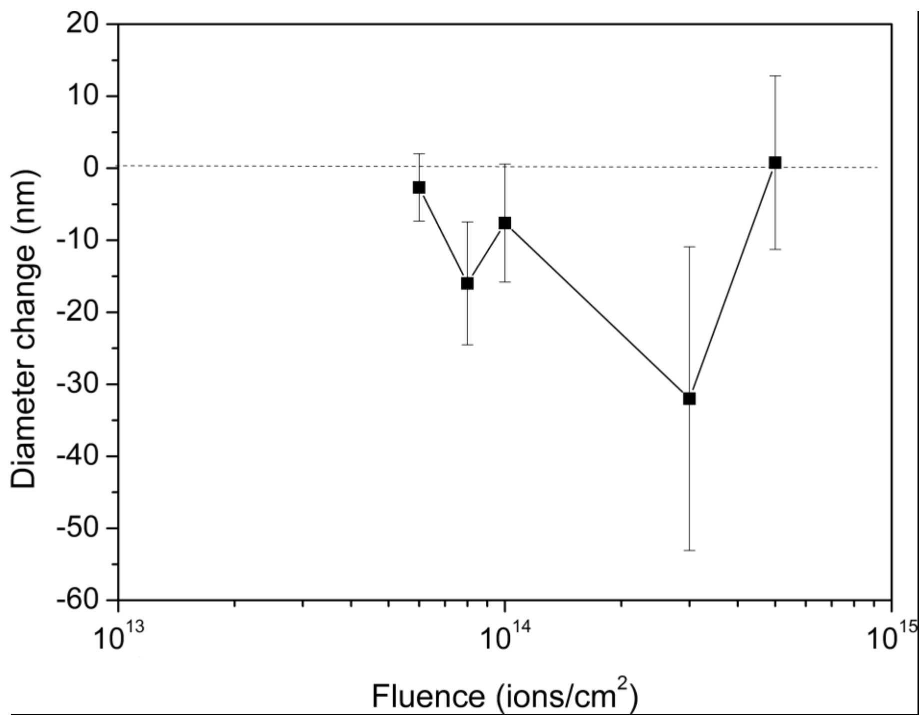

FIG. 4-4 Fluence dependence of diameter change in the nano-hole structure. The negative value of the diameter change indicates the shrinkage of the diameter.

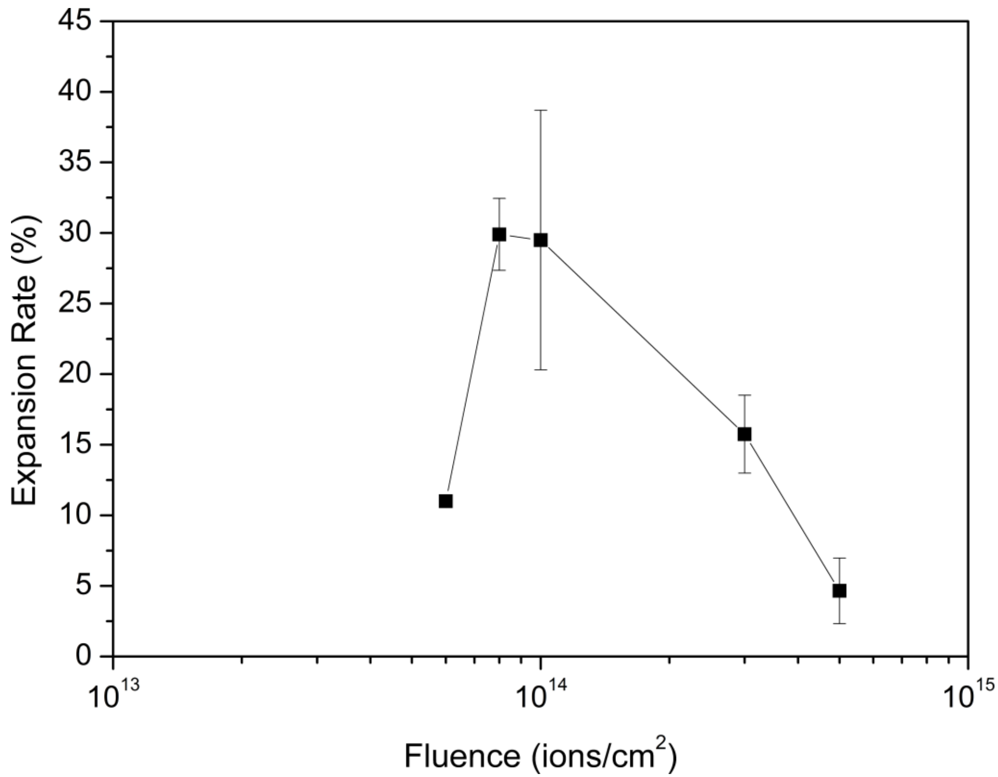

FIG. 4-5 Fluence dependence of the lateral expansion rate of a stripe structures, whose center piles with the width of 100 nm ~ 200 nm.

4.1.3 Lateral deformation as a function of structural size

In addition to fluence dependence, lateral deformation of crystalline nano-structure irradiated with low fluence ion beam also shows structural size dependence, as shown in Fig.4-6. Fig.4-6(a) indicate that width change decreases with structure size under the same irradiation conditions of fluence (8 x 10 ^{13} /cm^{2}) and energy (240 keV). The remarkable lateral deformation of stripe structures of ~ 200 nm is about 55 nm while that of stripe of 350 nm is only about 12 nm. The similar results can also be found in Fig.4-6(b). In contrast to Fig.4-6(a), Fig.4-6(b) indicate that only the lateral deformation of stripe of ~100 nm is remarkable at the relative higher fluence of 1 x 10 ^{14} /cm^{2}.

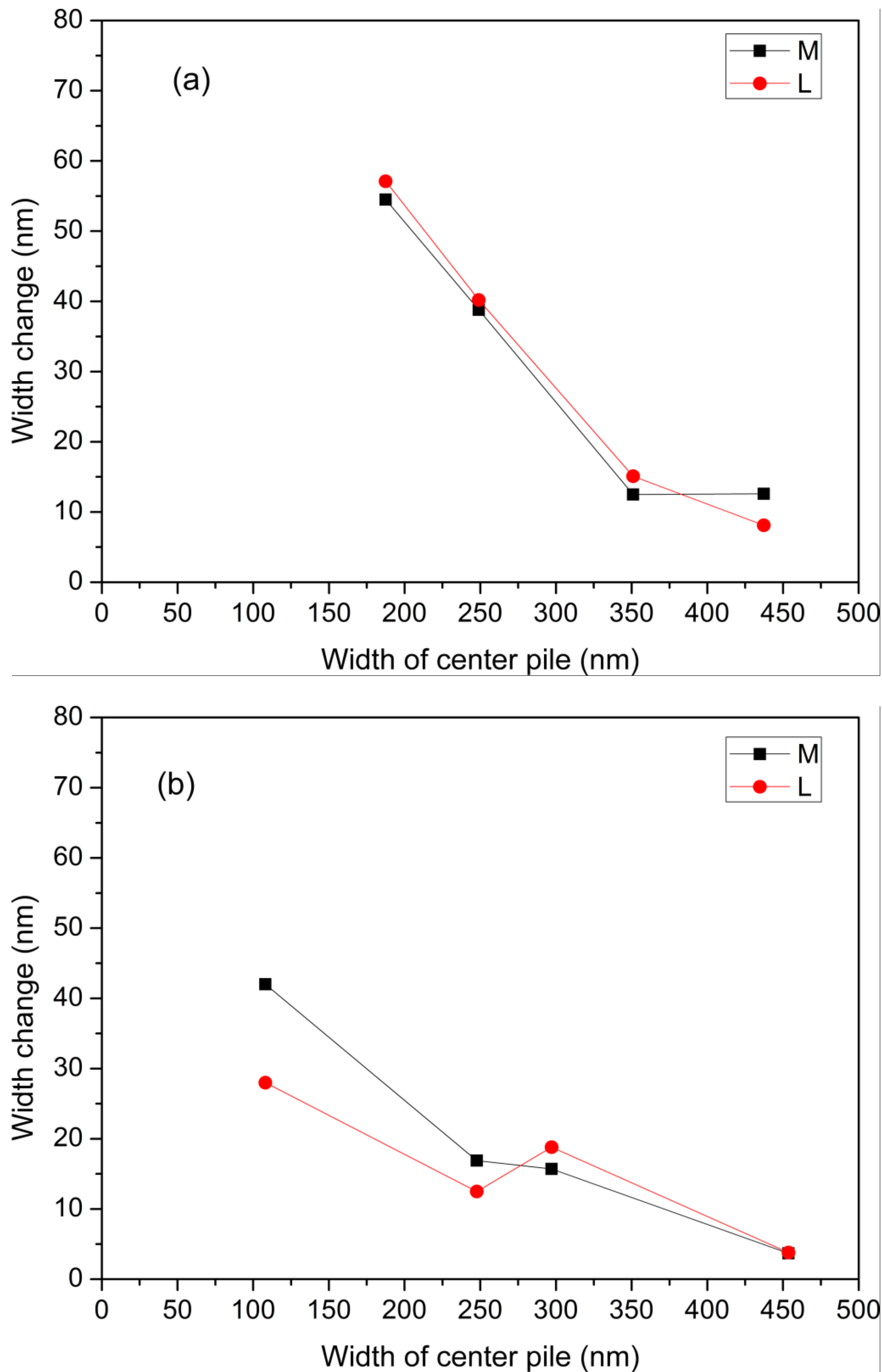

Fig. 4-6. Structure size dependence of the lateral deformation for stripe structures, (a) and (b) show the observed results with a fluence of 8×10^{13} and 1×10^{14} ions/cm^2, respectively.

4.2 Observation of Raman spectrum

4.2.1 Raman spectrum observed at different fluence

To investigate the inner change of *c*-Si induced by the Kr-beam irradiation, a Raman spectrum was observed at the flat region near the patterned region. Evolutional behavior of observed Raman spectrum with the fluence of the Kr-beam is shown in Fig. 4-7. A sharp peak at 520 cm^{-1}, which corresponds to *c*-Si, shrinks with the fluence. On the other hand, a peak at 510 cm^{-1}, which corresponds to a defective crystalline phase, appears in the spectrum for higher fluence. Also the broad peak placed at 480 cm^{-1}, which corresponds to *a*-Si, grows with the fluence, and becomes the dominant component in the spectrum for a fluence larger

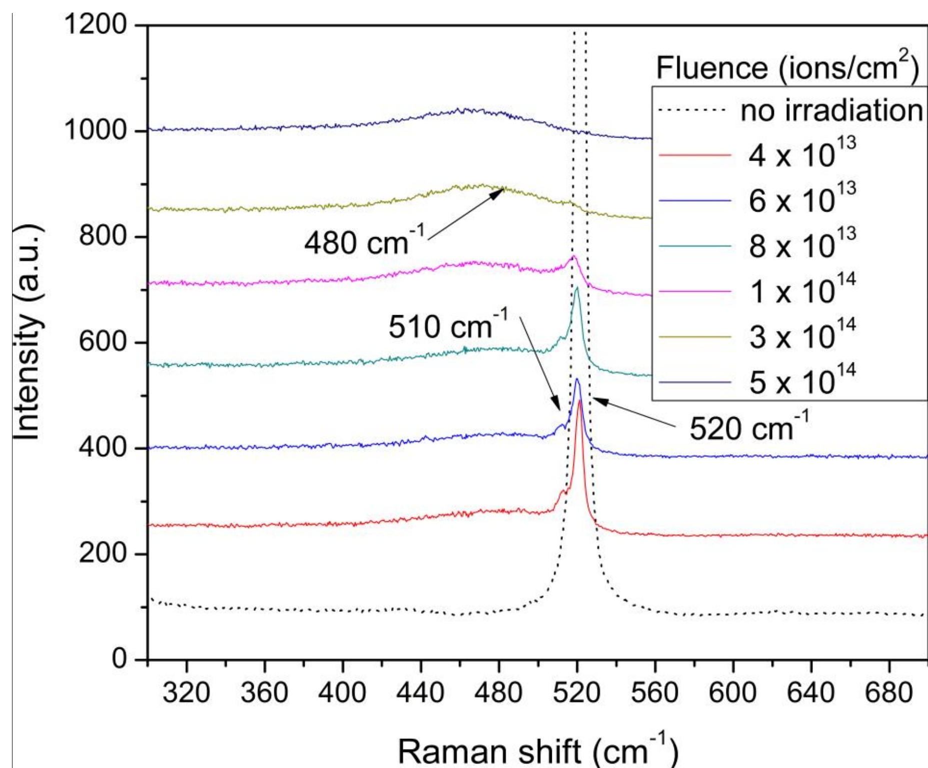

Fig. 4-7. Raman spectra of Si irradiated by Kr beam. The spectra for a virgin c-Si is also shown for a reference. The spectrum for each fluence is vertically displaced for clarity.

than 3 x 10^{14} ions/cm^2. Observed results of Raman spectrum indicates that amorphization of *c*-Si was induced by ion beam irradiation an important effect. Concerning the lateral deformation of nano-structures induced by ion-beam irradiation, shown in section 4.1, the

phase transition was expected to have a relation with lateral deformation.

4.2.2 Definition of amorphous fraction by using Raman spectrum

Based on an argument in 4.2.1, the amorphous fraction is one of important parameters that is related to the lateral deformation of surface nano-structure of *c*-Si. The crystalline volume fraction of a Si sample deduced from its Raman spectrum is expressed as[50]:

$$\varphi_c = (I_{520} + I_{510})/(I_{520} + I_{510} + I_{480}), \qquad (1)$$

where I_i is the area under the Gaussian distribution, whose center is located at i. As a semi-quantitative index, the amorphous faction, φ_a, is defined using φ_c as

$$\varphi_a = I_{480} /(I_{520} + I_{510} + I_{480}), \qquad (2)$$

4.2.3 Growing behavior of amorphous nature in Si crystal

To obtain amorphous fraction, Raman spectrum were deconvoluted by three-peak fitting to get each area I_i. Then, the amorphous fractions were calculated by equation (2) and results were shown in Fig. 4−8. The figure indicates that amorphous fraction increases with the fluence of Kr-beam and that the c-a phase change proceeds continuously in the fluence range between 6 x 10^{13} ions/cm^2 and 5 x 10^{14} ions/cm^2. Considering Fig. 4-3, the range of the Kr-beam fluence, at which the lateral deformation effect shows remarkable nonlinear fluence dependence, corresponds to the transitional range from the crystal phase to amorphous phase. The lateral deformation achieves the maximum (55 nm) at an amorphous fraction of about 85%. Also at higher fluence, the lateral deformation relaxes and returns to zero at an amorphous fraction of about 100%. As a result, Raman spectroscopy implies that the amorphization process of *c*-Si has an obvious relation with the lateral deformation of the *c*-Si nano-structure.

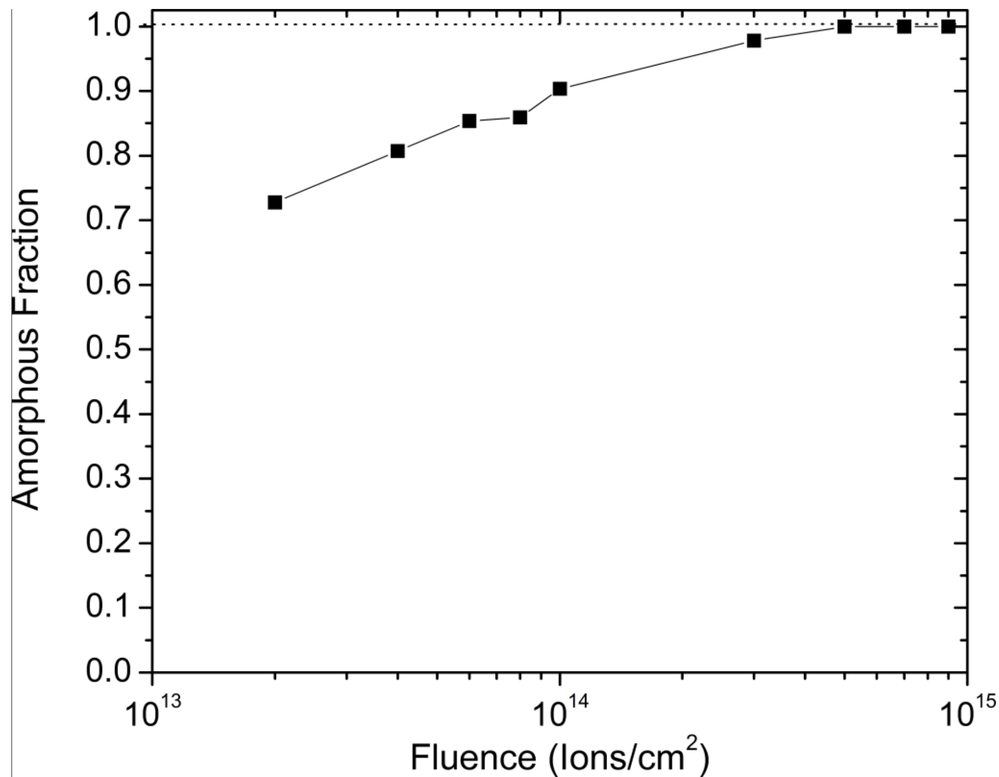

Fig. 4–8. Growth of amorphous fraction with the fluence of the Kr beam.

4.3 Observation of TEM image

4.3.1 Evolution of amorphous layer with fluence

Fig. 4-9 shows cross-sectional TEM images of the stripe structure irradiated by Kr-beam with three different fluences. In this figure, an amorphous layer is clearly recognized in the top and sidewalls of the stripe structure, and is separated from the crystalline region by an interface. The thickness of the amorphous layer grows with the Kr-beam fluence and reaches to 270 nm at the top of the center pile and 249 nm at the flat region for a fluence of 5 x 10^{14} ions/cm^2. This result indicates that the depth region of interest, 0 - 200 nm, evaluated by SRIM in 3.4, is completely amorphized for the higher fluence. The growing nature of the amorphous layer is consistent with the increase in the amorphous fraction, which was obtained from the Raman spectra. The figure also shows the differences in the thickness of the amorphous layer at the right and left sidewalls of the stripe structure. The tilt angle of Kr-beam irradiation from the normal of Si-surface would cause the asymmetric feature. In section 4.2, observed Raman spectra indicated the importance of the *c*-a phase change in

order to understand the lateral deformation effect on nano-structure. In the case of heavy-ion irradiation at low temperature (less than 200 ℃), the *c-a* phase change proceeds through the overlap of the isolated damaged region induced by ion-beam irradiation, and shows a heterogeneous nature [51]. Therefore, the amorphization induced by Kr-ion irradiation at RT is expected to be heterogeneous. In addiation, observed lateral deformation indicates structure size dependence, as described in section 4.1. To evaluate the heterogeneous nature of c-a phase change and contributions of the lateral size, high-resolution TEM images of center piles were observed for two structures with different lateral sizes, and shown in Fig's. 4-10 and 4-11.

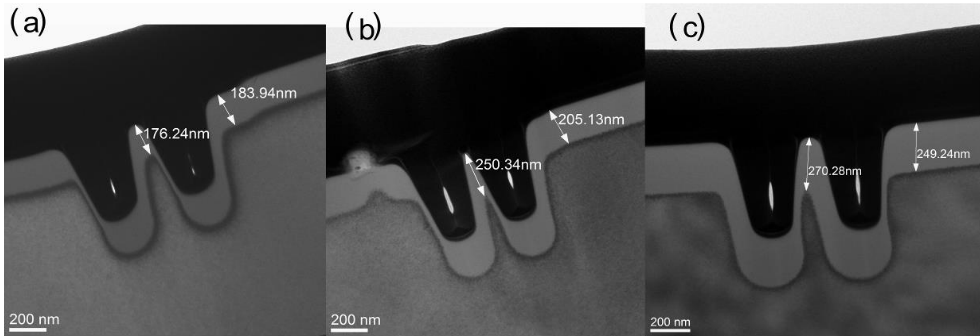

Fig. 4-9. Cross-sectional TEM images of stripe structures irradiated by Kr beam with fluences of (a) 8 x 10^{13}, (b) 1 x 10^{14}, and (c) 5 x 10^{14} ions/cm^2.

4.3.2 Crystalline and amorphous pockets observed at interface layer

Fig. 4-10(b), which is high-resolution image for a region indicated in Fig. 4-10(a), shows an interface in the stripe structure with the width of the center pile of ~100 nm irradiated with a fluence of 1 x 10^{14} ions/cm^2. The width of the crystalline region, which is located between two interfaces in the center pile, is about 40 nm. In Fig. 4-10(c), which is a higher-resolution image around the interface region, crystalline (amorphous) pockets [52], highlighted by black (white) circles, are found in the amorphous (damaged crystalline) region. According to ref. [52], *c-a* phase change induced by ion beam irradiation was discussed by means of amorphous and crystalline pockets. To confirm the nature of selected region, diffraction

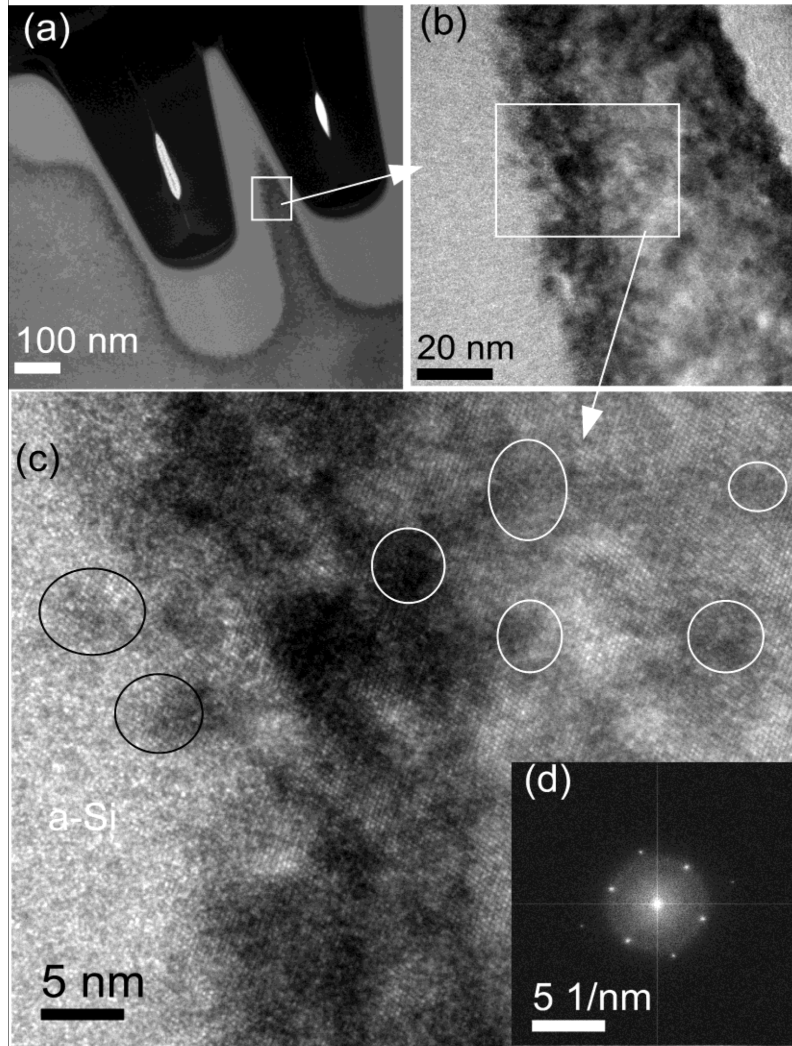

Fig. 4-10. TEM images of stripe structures with the width of the center pile of ~100 nm, irradiated with a fluence of 1 x 10^{14} ions/cm^2; (a), (b), and (c) are cross-sectional images of different resolution. The rectangles in (a) and (b) indicate the observed regions for higher resolution. Amorphous pockets and crystalline pockets are highlighted by white circles and black circles, respectively. (d) Fourier transform of (c).

pattern was calculated by means of Fourier transform. A damaged crystalline region is confirmed to be the coexistence of the diffraction pattern and the continuous circle in Fig. 4-10(d).

Fig. 4-11(a) shows the cross section of the stripe structure with the width of the center pile of ~ 450 nm irradiated with a fluence of 1 x 10^{14} ions/cm^2. The width of the crystalline region between the two interfaces is ~ 300 nm, which is much larger than that of the width

of ~100 nm. Fig. 4-11(b) is a high-resolution image of the interface region indicated in Fig. 4-11(a). Fig. 4-11(c), observed around the interface region, shows an existence of crystalline (amorphous) pockets, highlighted by black (white) circle, as in Fig. 4-10(c). A continuous circle found in Fig. 4-11(e), which is a diffraction pattern obtained in the region defined in Fig. 4-11(b), indicates incomplete amorphization and the existence of a strain in the system. In contrast, the diffraction pattern in Fig. 4-11(f) shows that the region under the interface keeps the crystal nature.

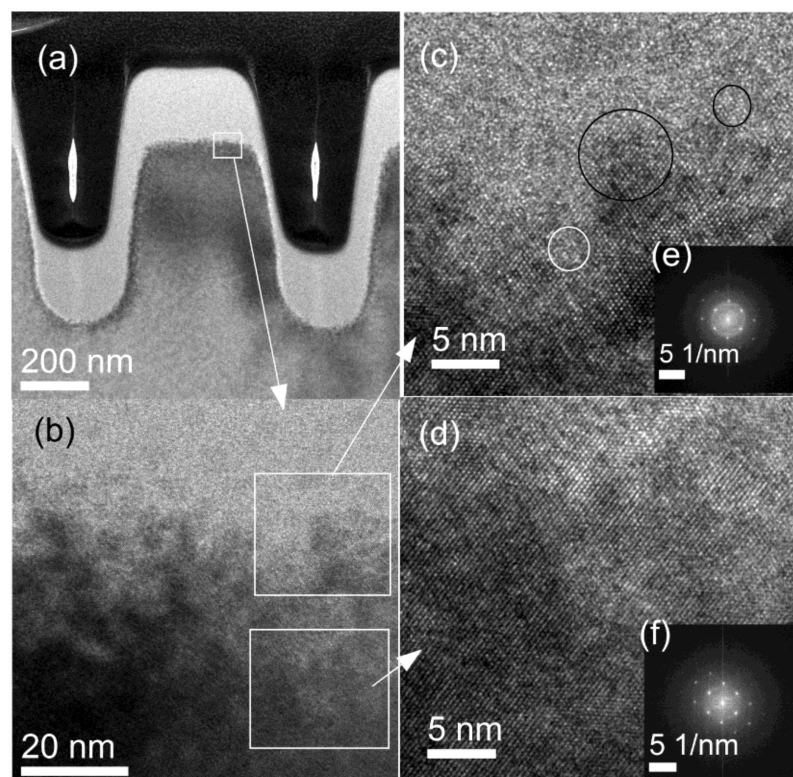

Fig. 4-11. TEM images of stripe structure with the width of the center pile of ~ 450 nm, irradiated with a fluence of 1 x 10^{14} ions/cm^2; (a), (b), and (c) are cross sectional image of the center pile region in different resolutions; (e) and (f) are Fourier transforms of (c) and (d), respectively.

In both TEM images of Fig. 4-10 and Fig. 4-11, crystalline/amorphous pockets, which indicated heterogeneous amorphization, are found in the vicinity of the interface. And the

width of the crystalline region, which is placed between two interfaces in the center pile, changes according to the lateral size of the stripe structure. Decreasing the lateral size, the two interfaces approaches to remove the crystal region in the center pile.

4.4 Mechanism of lateral deformation induced by low fluence ion beam irradiation

4.4.1 Contribution of sputtering effect

The sputtering effect is another important contribution to cause the lateral deformation. Considering the sputtering rate and its incident angle dependence, which are evaluated by SRIM, the contribution of sputtering effect to the lateral deformation under the present irradiation condition is calculated to be less than 0.64 nm even at the maximum fluence of 5×10^{14} ions/cm^2. Therefore, the sputtering effect is not considered in the following argument.

4.4.2 Comparison with irreversible deformation

The presently observed deformation, which was induced by Kr-beam irradiation with low fluence, is compared with the previously observed deformation. The growing and shrinking of the lateral deformation was observed in the fluence range, within which the crystalline phase continuously changes to the amorphous phase. The effective fluence range for the lateral deformation is significantly lower than that for irreversible deformation, which was observed in a-Si micro/nanostructure [13, 14]. The irreversible deformation for amorphous material is called plastic deformation, and is successfully explained by a viscoelastic model proposed by Trinkaus and Ryaznov [53]. And, the presently observed deformation is promoted for structures with small lateral size, and suppressed for those with large lateral size. The size effect on plastic deformation was observed for spherical SiO_2 colloid [24] and ascribed to a nonhydrostatic stress distribution by surface curvature. Because initial phases

and/or morphological shapes as well as irradiation parameters are different, it is difficult to apply those previous models to explain the presently observed lateral deformation. In the present studies, initial structures are in the crystalline phase as described in section 4.3. The amorphous/crystalline pockets and internal stress were observed in TEM images for stripe structures, in which a remarkable lateral deformation was observed. Therefore, the fluence dependence of the lateral deformation is considered by means of the amorphous/crystalline pockets.

4.4.3 Contribution of amorphous/crystalline pockets

The cascade localization induced bias (CLIB) model, proposed by Yoshiie *et al.* [54] to explain the behaviors of defects in the lattice system, indicates that defects induced in the Si lattice by Kr-beam irradiation would be absorbed by boundaries between amorphous/crystalline pockets and their surroundings. This absorption stimulates the growth of amorphous pockets and shrinkage of the crystalline pockets. Also, when amorphous pockets grow to overlap with others, they would combine and contributions of boundaries to absorb defects are suppresses. Based on this idea, the fluence dependence can be qualitatively understood as follows. In the case of lower fluence, amorphous pockets are produced and grow to promote a heterogeneous nature with the fluence of Kr beam. Then the internal stress, which promotes the expansion effect, increases. On the other hand, in the case of higher fluence, amorphous pockets start combining with others with increasing the fluence of Kr beam. Then the internal stress decreases.

4.4.4 Contribution of lateral size

Considering observed TEM images, the following naive model is a possible candidate to explain the contribution of lateral size to the lateral deformation. In the case of a smaller lateral size, the crystalline region between two interfaces in the center pile reduces, and the major part of the center pile is occupied by the amorphous region. Therefore, contributions of stress induced by the heterogeneous nature would become obvious in the whole region

between the interfaces in the left and right sidewall, and promote an expansion along the lateral direction. In contrast, in the case of the larger lateral size, the contribution of the crystalline region, which tends to keep its form, becomes prior. Therefore, the lateral deformation effect would be suppressed by the crystalline region compared with structures of smaller lateral size.

4.5 Conclusion

In conclusions, a deformation of taper-shaped Si structures along the lateral direction has been successfully achieved firstly by irradiating Kr beam of 240 keV. The observed results have shown that the lateral deformation depends on the lateral size of taper-shaped Si structure as well as the fluence of Kr beam. The typical fluence of a 240 keV Kr-beam employed to provide lateral deformation is about 1 x 10^{14} ion/cm^2. This fluence is much lower than the typical fluence of ion beams, which is needed to provide plastic deformation in amorphous materials. The amorphous/crystalline pockets, which were observed with stress in the lattice structure, can provide a consistent qualitative explanation for observed lateral deformation and its fluence dependence. The suppression effect on the lateral deformation, which would originate from crystalline region between two interfaces in the center pile, provides a possible explanation for the structure size dependence. However, further investigations are needed to confirm the reliability of this idea. In addition, the contributions of irradiation energy and ion species will be performed in next studies.

5 Modification of mechanical properties of Si crystal

Previous researches have experimentally confirmed the possibility of controlling the swelling height on flat *c*-Si surface by the means of ion beam irradiation [20]. Lateral deformation of nanostructures was successfully achieved in section 4. These controllability in two direction will help further development of the fabrication process of 3D structures. One of important applications of 3-D nanostructures is MEMS. Mechanical properties are

one of important factors of MEMS. Therefore, evaluation of the effect of ion beam irradiation on Si materials is necessary. In this section, the mechanical properties, hardness and Young's modulus, have been investigated by means of nanoindentation.

5.1 Measurement of mechanical properties by means of nanoindentation

Fig. 5-1 shows the load/unload curves obtained by means of indentation for *c*-Si irradiated with Kr-beam. The obvious pop-out event are identified in unloading process, as shown in Fig. 5-1. In load curves, small but obvious pop-in events are identified at a displacement about 100 nm for the curve of 1×10^{14} ions/cm^2 and about 140 nm for the curve of 5×10^{14} ions/cm^2 in insets. The events of pop-in and pop-out indicated the phase transition in the loading process and the unloading process, respectively. The pop-in events were expected to be associated with discontinuity of mechanical properties.

In this study, the Young's modulus and hardness were mainly characterized as the mechanical properties of silicon materials. In order to obtain the Young's modulus and hardness before and after implantations with 1×10^{14}, 5×10^{14} ions/cm^2 240 keV Kr-ion, nanoindentations were performed with CSM mode described in section 3.3.4. And the results, as shown in Fig. 5-2, were the average of ten indentations with error bars representing the standard deviation. In Fig. 5-2, both of Young's modulus and hardness modified by Kr-beam irradiation decrease with fluence. The Young's modulus of *c*-Si before Kr-beam irradiation is 176.1 GPa, which is close to that is reported for *c*-Si, 160-180 GPa [55, 56]. After Kr-beam irradiation of 1×10^{14}, 5×10^{14} ions/cm^2, the mean Young's modulus, which were defined in a depth range of 50 – 60 nm, were 163.4 GPa and 158.9 GPa, respectively. The change in Young's modulus can be recognized by the difference between curves in the typical depth profile showed in Fig. 5-2(a). Smaller value of Young's modulus is observed at the irradiated surface and gets close to the value before irradiation.

For the case of hardness, the similar behaviour of fluence dependence of depth profile is found in Fig. 5-2(b). The hardness of *c*-Si before ion beam irradiation is 13.0 GPa, and

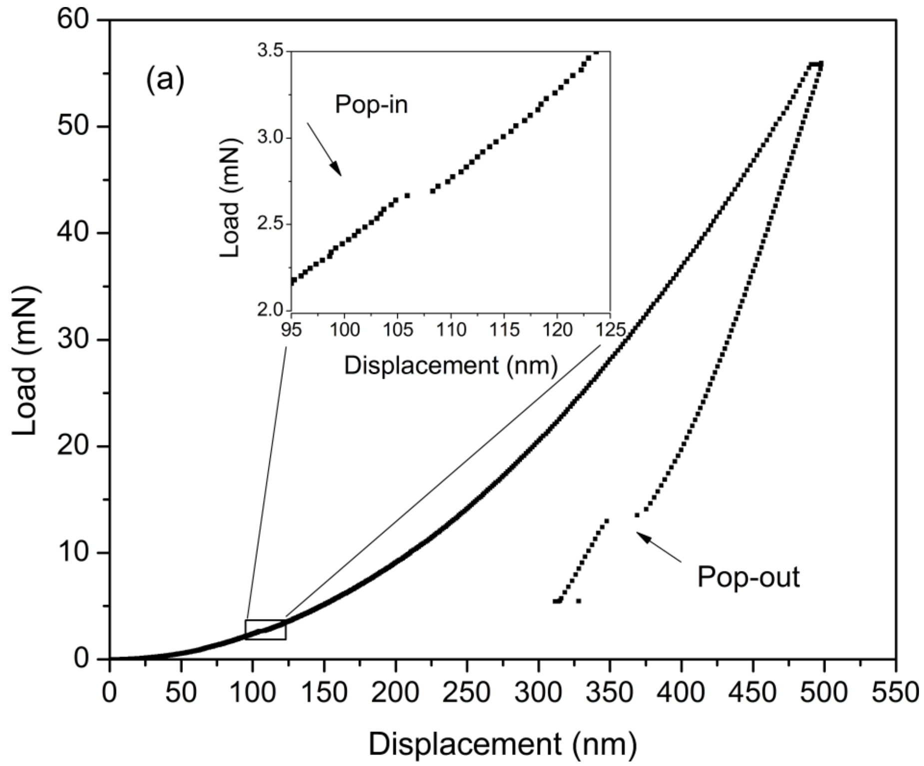

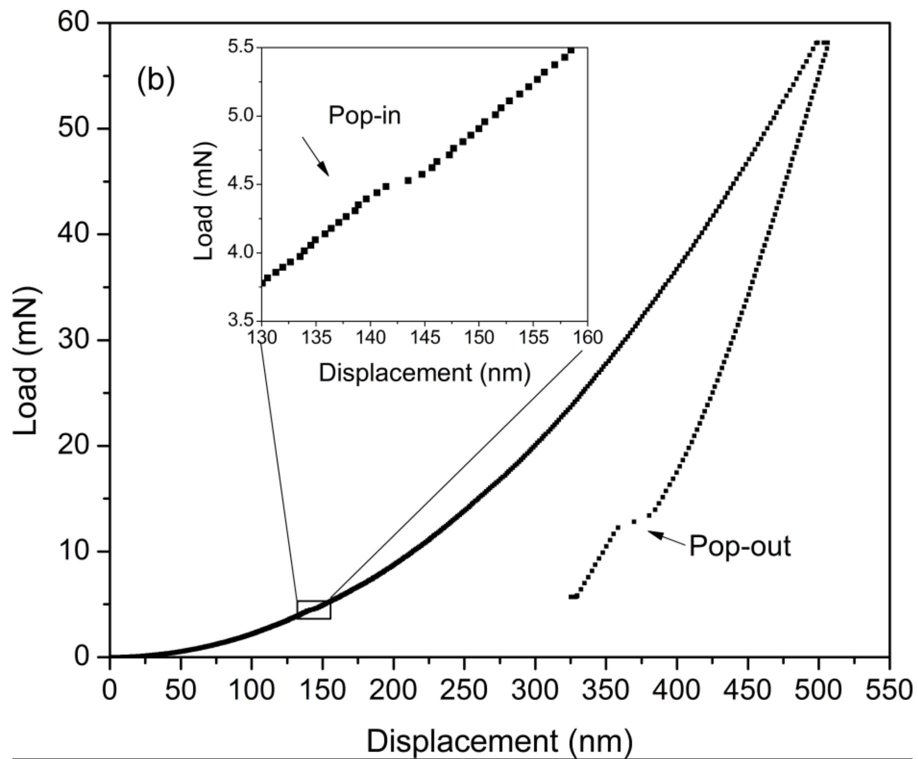

Fig. 5-1 Typical load/unload curves for *c*-Si irradiated by Kr-beam with a fluence of (a) 1×10^{14} ions/cm^2 and (b) 5×10^{14} ions/cm^2. Pop-out and pop-in, which are indicated in insets, are identified in unloading and loading process, respectively.

that after Kr-beam irradiation, defined in the same depth range of Young's modulus, is 11.8 and 10.8 GPa for the fluence of 1×10^{14} and 5×10^{14} ions/cm^2, respectively. The change in hardness can be easily recognized by the difference between curves in the typical depth profile shown in Fig. 5-2(b).

To extract contribution of the fluence to mechanical properties, changes in Young's modulus (⊿Young's modulus) and hardness (⊿Hardness) from those of unirradiated *c*-Si were calculated as shown in Fig. 5-3. Here, negative values indicate decrease compared with before irradiation. Fig. 5-3(a) shows ⊿Young's modulus decreases with depth. In the case of lower fluence of 1×10^{14} ions/cm^2, ⊿Young's modulus gradually decreases from 26 to 0 GPa with depth increasing from 0 to ~ 180 nm. In the case of higher fluence of 5×10^{14} ions/cm^2, ⊿Young's modulus gradually decreases from 30 to 0 GPa with depth increasing from 0 to ~ 240 nm. Therefore, the depth of a layer, whose Young's modulus is modified, also shows fluence dependence. At the same modified depth, ⊿Young modulus induced by higher fluence is larger than that induced by lower fluence. Fig. 5-3(b) shows the similar behaviour with Young's modulus.

In the case of lower irradiation fluence of 1×10^{14} ions/cm^2, ⊿Hardness decreases from 2.7 to 0 GPa with depth increases from 0 to 270 nm. In case of higher fluence of 5×10^{14} ions/cm^2, ⊿Hardness decreases from 5.2 to 0 GPa with depth increases from 0 to more than 300 nm. Therefore, the depth of a layer, whose Hardness is modified, also shows fluence dependence. And at the same depth, hardness change induced by higher fluence is larger than that induced by lower fluence.

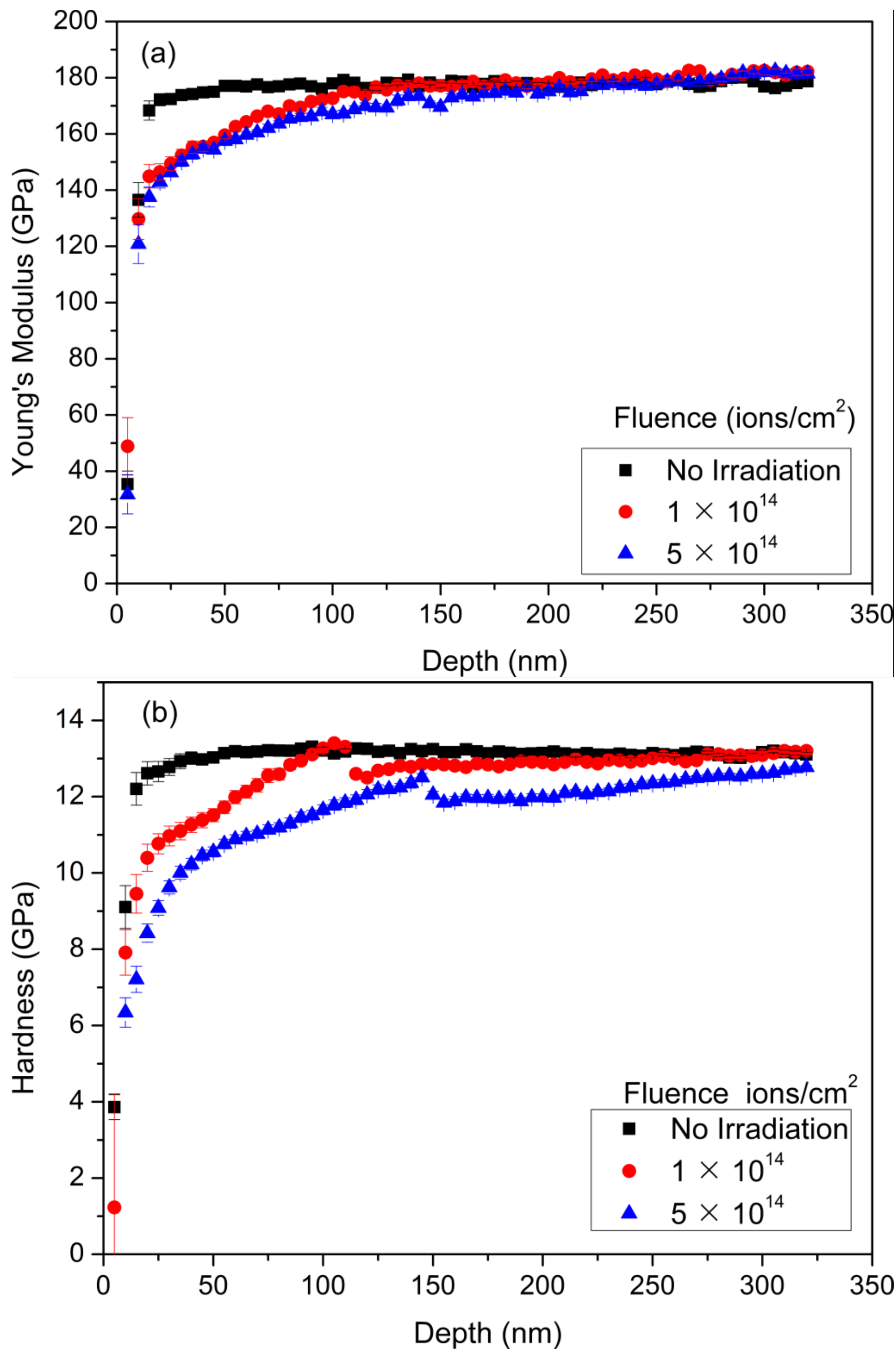

Fig. 5-2 Young's modulus (a) and hardness (b) of c-Si obtained from continuous measurements before and after irradiation of 240 keV Kr-beam.

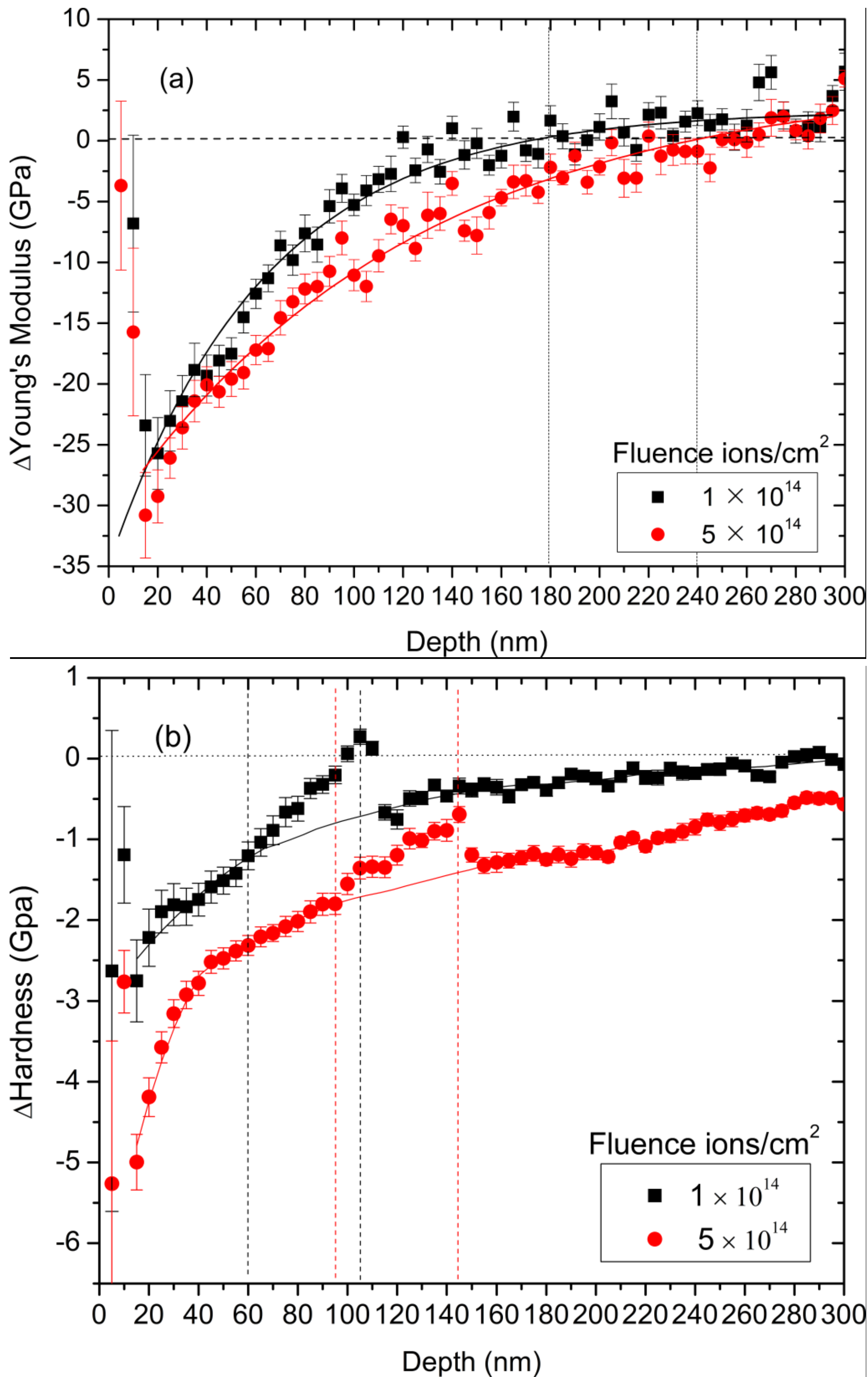

Fig. 5-3 Changes in (a) Young's modulus and (b) hardness of *c*-Si induced by irradiation of Kr-beam. Solid lines show guidance for eyes.

By comparing the depth profiles between ⊿Young modulus and ⊿Hardness, the depth of a modified layer for hardness was larger than that for Young's modulus under the same irradiation condition. This result reveals that the hardness was more sensitive to damage induced by ion beam irradiation than Young's modulus. In addition, there is a dip in each curve of depth profile for hardness, at 105 nm for the curve of 1×10^{14} ions/cm^2 and at 145 nm for the curve of 5×10^{14} ions/cm^2. A noticeable behaviour of sudden decrease in hardness change was found in the depth range of 60 – 105 nm for the curve of 1×10^{14} ions/cm^2 and 95 – 145 nm for the curve of 5×10^{14} ions/cm^2. The dip is not found in that for Young's modulus.

5.2 Observation of Raman spectrum

Fig. 5-4 shows the evolutional behavior of the Raman spectrum with the fluence of Kr-beam. A sharp peak at 520 cm^{-1}, which corresponds to c-Si, shrinks with the fluence. On the other hand, the broad peak placed at 480 cm^{-1}, which corresponds to a-Si, grows with fluence, and becomes the dominant component in the spectrum for a fluence of 5 x 10^{14} ions/cm^2. This result indicate that amorphous fraction increased with irradiation fluence and the continuous amorphous layer is expected to be formed at irradiated surface. Therefore, phase transition is related to observed change in mechanical properties.

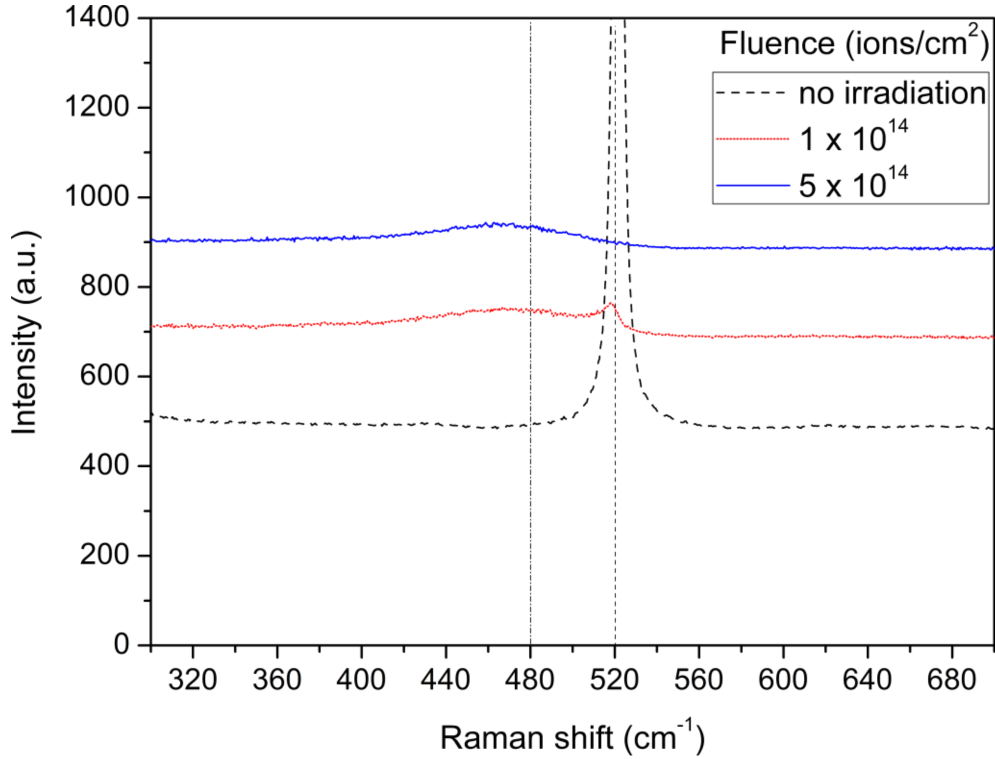

Fig. 5-4 Raman spectra of Si before and after irradiation of Kr-beam. The spectrum for each fluence is vertically displaced for clarity.

5.3 Observation of TEM image

TEM images shown in Fig.5-5 (a) indicates that the thickness of the amorphous layer formed in *c*-Si surface reached 199 nm after Kr-beam irradiation with the fluence of 1×10^{14} ions/cm^2. When the fluence increased up to 5×10^{14} ions/cm^2, the corresponding thickness of the amorphous layer increased further to 240 nm, as shown in Fig. 5-5(b).

Fig. 5-6(a) shows the amorphous-crystal interface of *c*-Si irradiated with a fluence of 1×10^{14} ions/cm^2. A continuous circle found in Fig. 5-6(c), which was obtained from the region defined in Fig. 5-6(a), indicates complete amorphization. In Fig. 5-6(d), a diffraction pattern with continuous circle, obtained from the region defined in Fig.5-6(a), indicates incomplete amorphization. The diffraction pattern in Fig. 5-6 (e) indicates that the region, which located beneath the transition region, keeps crystal nature. In Fig. 5-6(b), which is a

higher resolution image around the transition region, amorphous pockets, highlighted by white circles, are found. Small misorientation regions, highlighted by black circles, are found in the amorphous region, as also found in Fig. 5-6(a).

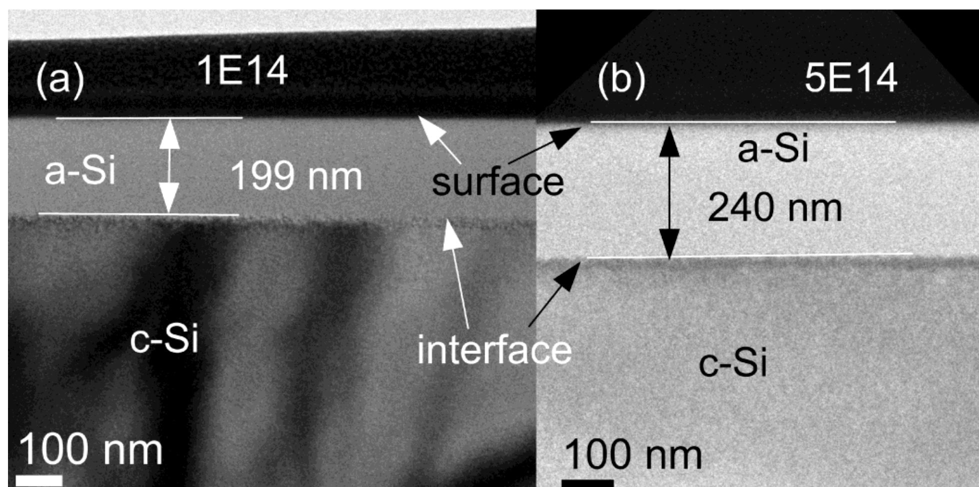

Fig. 5-5 Cross-sectional TEM images of Si irradiated by Kr-beam with fluences of (a) 1 x 10^{14} and (b) 5 x 10^{14} ions/cm^2.

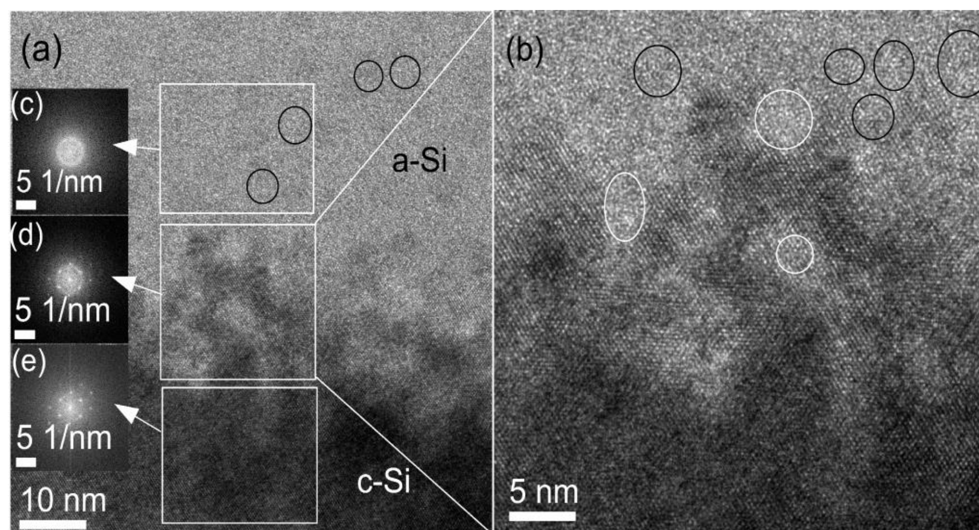

Fig. 5-6 TEM images around the interface between amorphous and crystalline region, irradiated with a fluence of 1×10^{14} ions/cm^2. (a) is cross sectional image in low resolution, and (b) is cross sectional image in higher resolution. (c), (d), and (e) are Fourier transforms of regions marked in (a).

5.4 Measurement of RBS-C spectrum

Fig. 5-7 shows the density distributions of defect in *c*-Si obtained from RBS-C-spectra. The density was calculated from RBS-C spectrum through a procedure described in ref. [57]. The saturation of the defect density corresponds to the amorphous phase. According to the ref. [58], to reduce the ambiguities induced by the energy straggling and system resolution, the full width at half maximum (FWHM) of defect distribution was defined as the thickness of the amorphous layer, as shown in Fig. 5-7. According to this definition, the thickness of the amorphous layer, shown in Fig. 5-7, reached 205 nm, and 250 nm for the fluence of 1×10^{14} ions/cm^2 and 5×10^{14} ions/cm^2 , respectively. The results are consistent with the thickness of amorphous layer observed by TEM.

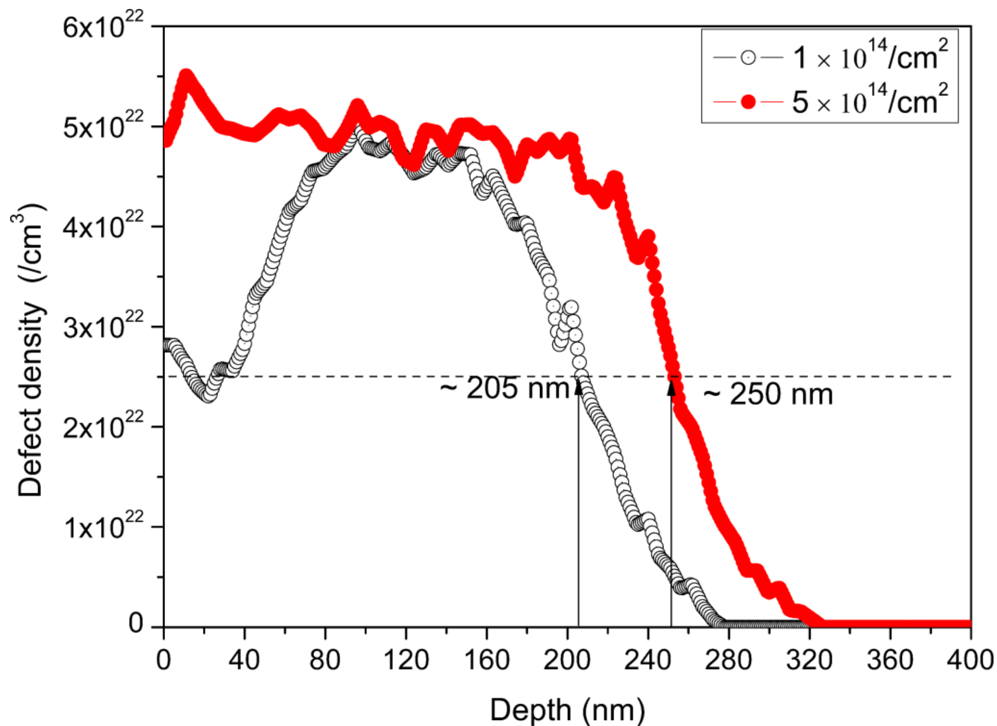

Fig. 5-7 Density distribution of defect in irradiated *c*-Si obtained from RBS-C spectra.

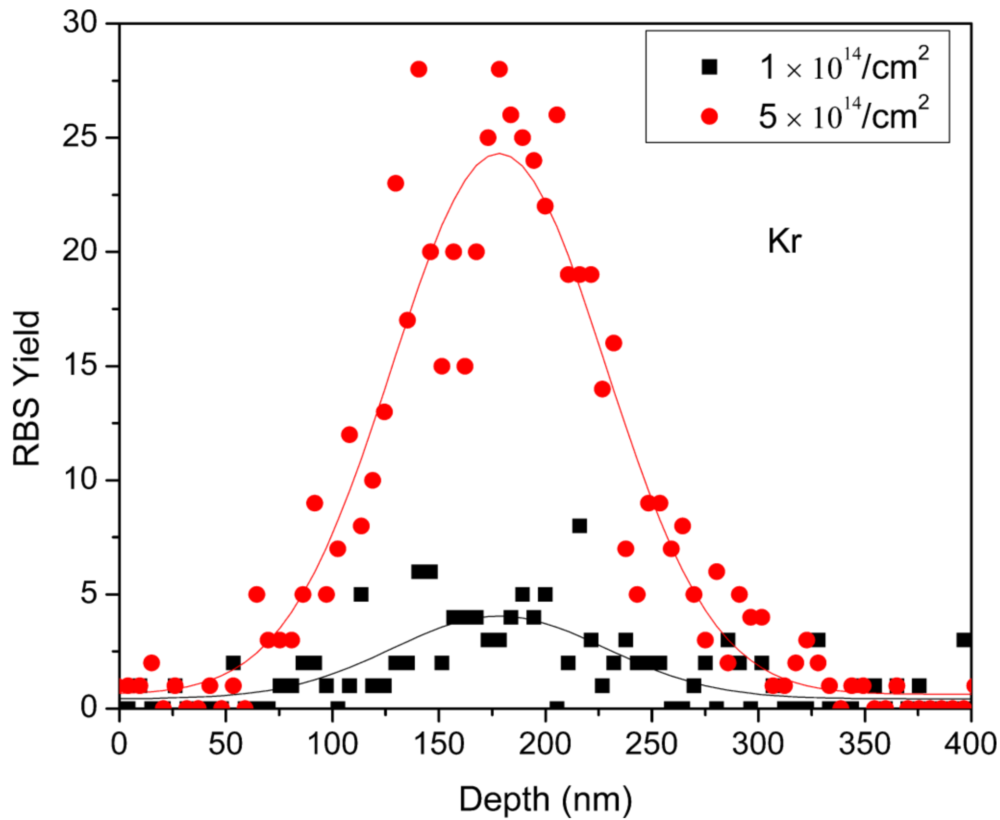

Fig. 5-8 Distributions of Kr in c-Si measured by RBS-C method. Solid lines are the fitted results by means of Gaussian function.

The density distribution of defects in irradiated c-Si shown in Fig. 5-8 indicates that the distributions of defects cover a depth range from 0 to 277 nm at a fluence of 1×10^{14} ions/cm^2 and a depth range from 0 to 325 nm with a fluence of 5×10^{14} ions/cm^2. Distributions of Kr atom in irradiated c-Si, shown in Fig. 5-8, are close to a Gaussian-like distribution. The center and FWHM of the distribution for both fluence agree and are about 180 and 120 nm, respectively. Therefore, major part of Kr-ions, ~ 75 %, stops at the depth region between 120 and 240 nm.

5.5 Calculation of amorphous layer by SRIM

To confirm the thickness of the amorphous layer, the behavior of Kr-ions into crystal silicon was simulated by using SRIM program. According to ref. [59], a threshold value for complete amorphization of c-Si is 5.0×10^{23} eV/cm^3. It means that the minimum deposited energy to

recoils per unit length, which is required to cause full amorphization, are 50 eV/ion/Å for the fluence of 1×10^{14} ions/cm^2 and 10 eV/ion/Å for the fluence of 5×10^{14} ions/cm^2. Based on this results, the evaluated thickness of an amorphous layers for the fluence of 1×10^{14}, 5×10^{14} ions/cm^2, as shown in Fig. 5-9, are 162 and 210 nm, respectively.

The above results obtained from SRIM calculation and TEM observations indicate that the thickness of the amorphous layer formed in *c*-Si surface increase with increasing the fluence of Kr-beam. However, the thickness calculated by SRIM is relatively thinner than that provided from TEM images.

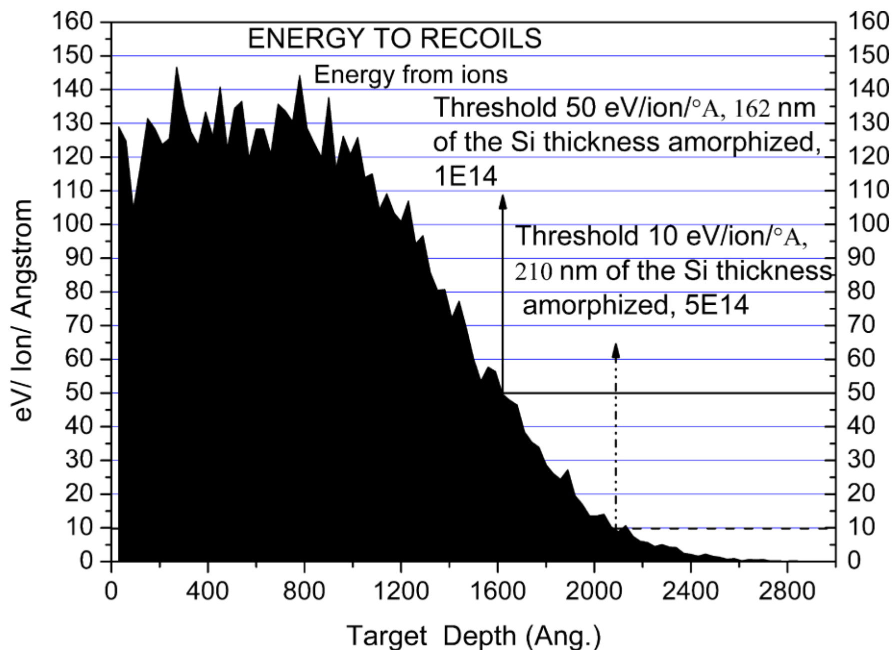

Fig.5-9 Energy to recoiled Si calculated by SRIM. The graph indicates that the thicknesses of completely amorphized layer for the fluence of 1 x 10^{14} and 5 x 10^{14} ions/cm^2 are 162 nm and 210 nm, respectively.

5.6 Effect of irradiation damage on mechanical properties

5.6.1 Fluence dependence

The experimental results indicated the importance of irradiation damage to understand the modification of mechanical properties. Firstly, changes in mechanical properties indicate fluence dependence as shown in Fig. 5-2. The depth of modified layer increases with fluence and mechanical properties decrease with fluence at the same modified depth. In case of Young's modulus, the depths of modified layer, shown in Fig. 5-2(a), 180 nm for the fluence of 1×10^{14} ions/cm^2 and 240 nm for the fluence of 5×10^{14} ions/cm^2, are consistent with the observed thicknesses of the amorphous layers, shown in Fig. 5-5, 199 nm for the fluence of 1×10^{14} ions/cm^2 and 240 nm for the fluence of 5×10^{14} ions/cm^2, provided by TEM

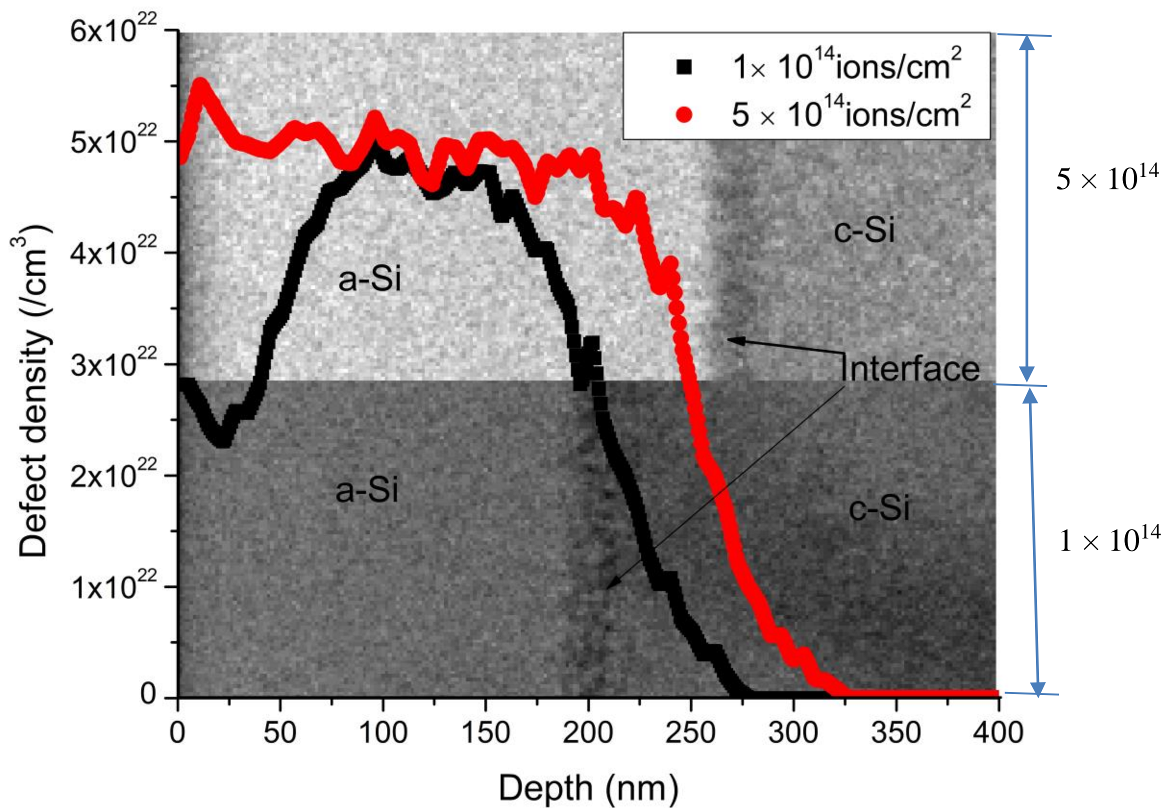

Fig. 5-10 Density distribution of defect obtained from RBS-C spectra with TEM images.

observation. Furthermore, the thickness of amorphous layer obtained from SRIM calculation, TEM observation, and RBS-C measurement indicate similar fluence dependence. And the fluence dependence is consistent with the behaviors of change in Young's modulus, as shown in Figs. 5-10 and 5-11. Therefore, it is suggested that the phase transition is strongly related to the modification of the Young's modulus. The network of a-Si was reported to have short and medium range order [35]. Pantchev *et al.* [36] reported that the decrease in Young's modulus of irradiated a-Si is associated with the structure change, such as the increase in the Si-Si bond angle deviation. The induced structural disorder in the silicon network, which are associated to the variation of the short and intermediate range order, leads to a significant decrease in the mechanical stress [37]. The irradiation effect observed as the decrease in Young's modulus is ascribed to the increase in the short-range order of the silicon network. And the reduced Young's modulus observed for irradiated *a*-Si could be related to the increase in the Si-Si bond angel deviations [15]. Therefore, crystalline-to-amorphous phase transition indicates the long-range order of Si network transforms to short-range order of Si network. As shown in Fig 5-6, lattice of crystalline silicon can be found in the crystalline region while some small misorientation regions, highlighted by black circles, can be found in the amorphous region. It is suggested that the decrease in Young's modulus is associated with the induced decrease in the order of Si network in the process of crystal to amorphous phase transition. According to the above idea, the origin of the decrease in Young's modulus with fluence is expected to be from the decrease in the short range order of Si network by Kr-beam irradiation.

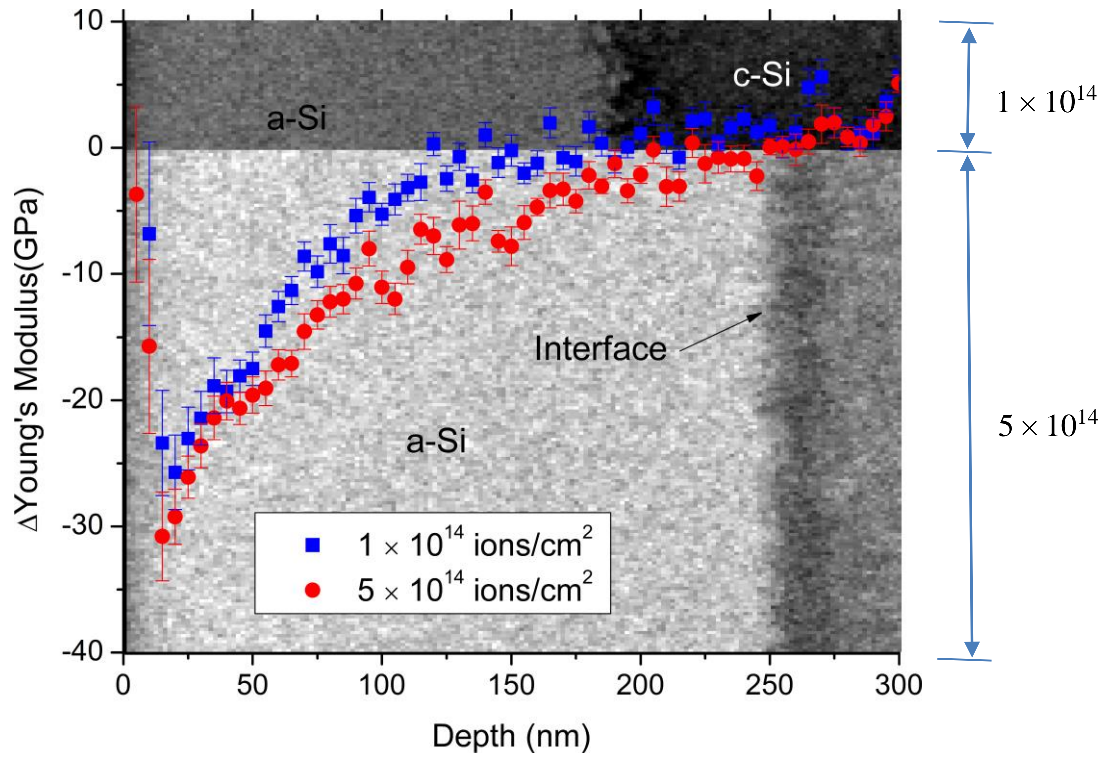

Fig. 5-11 Changes in Young's modulus with TEM images

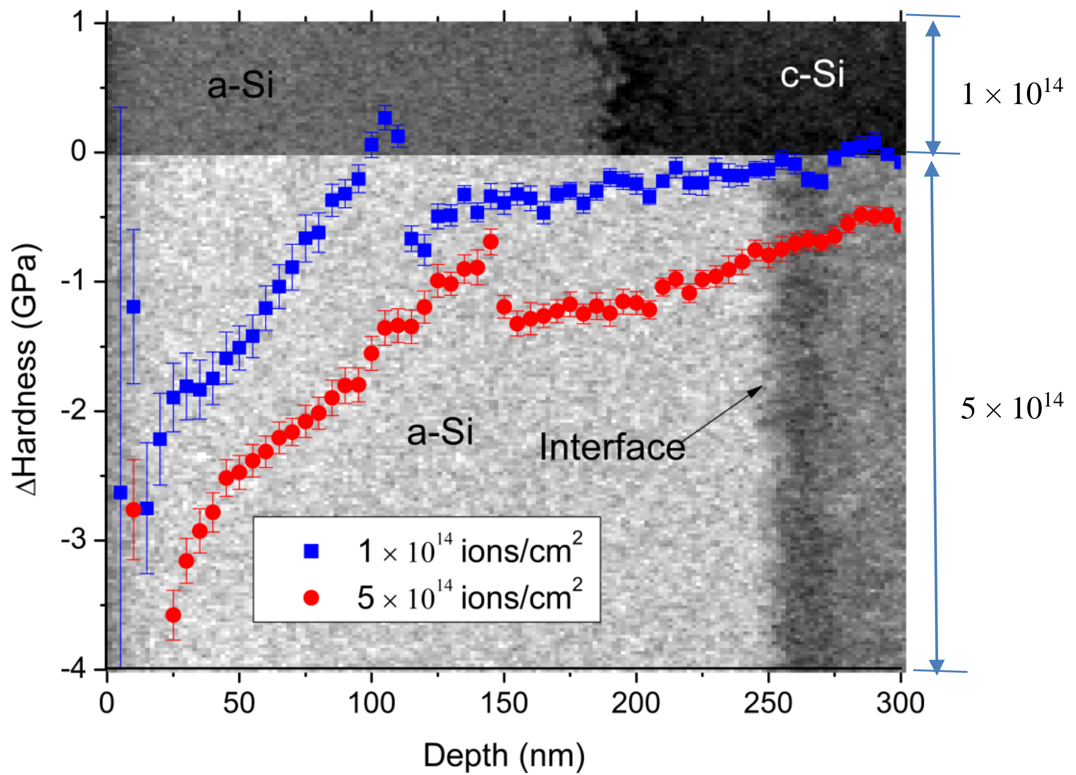

Fig. 5-12 Changes in hardness with TEM images

In the case of hardness, the depth of modified layer, shown in Fig. 5-2(b), is 270 nm and 320 nm for the fluence of 1×10^{14} ions/cm^2 and 5×10^{14} ions/cm^2, respectively. This result is consistent with the range of defects distribution, shown in Fig. 5-7, 0 ~ 277 nm and 0 ~ 325 nm for the fluence of 1×10^{14} ions/cm^2 and 5×10^{14} ions/cm^2, obtained from RBS-C measurement. These results indicate that the modification of hardness corresponds with defects distribution induced by Kr-beam irradiation. The range of defect distribution measured by RBS-C provides consistent results with the modified depth range of hardness, as shown in Figs. 5-10 and 5-12. In addition, G. Pfanner *et al.* [38] reported that dangling bond defect in a-Si, which corresponding to a network defect, is generated at suitable geometric distortions in the network while the dangling bond in crystalline silicon is usually related to the presence of a vacancy. According to ref. [15], decrease in hardness induced by ion implantation is related to the increase in density of dangling bond, caused by atom displacements in the target. Therefore, a high concentration of defects, such as vacancies, in *c*-Si results in the decrease in long-range order of Si network to form a continuous amorphous layer and a great number of dangling bonds are generated at the same time. According to ref. [39, 40], the density of dangling bond is about 10^{19} – 10^{20} cm^{-3} in the hydrogen-free *a*-Si. In case of relatively lower concentration of defects, a continuous amorphous layer is not formed, however, the defects still generate a good many of dangling bonds, whose density is lower than that in the continuous amorphous region. In addition, it was reported that the indentation process induced a phase transition to cause plastic deformation via plastic flow and that the plastic flow is promoted by high density of dangling bond defects in ref. [41, 42]. Based on those reports, the density distribution of dangling bonds would correspond with the that of defects, as shown in Fig. 5-7. Therefore, the fluence dependence of hardness could be understood based on the behaviors of dangling bonds distribution, which corresponds with the distribution of defect. And the decrease in hardness with fluence is ascribed to the irradiation-induced increase in defect density, which determines the dangling bond density.

5.6.2 Comparison between changes in Young's modulus and hardness

In this section, I will compare the depth profiles between *Δ*Young's modulus and *Δ*hardness. The present results indicate that the hardness is more sensitive to the damage induced by ion-beam irradiation while the Young's modulus sensitive to the crystalline-to-amorphous phase transition. Based on the analysis in previous section, *Δ*Young's modulus is related to the change in order degree of Si network. On the other hand, changes in hardness is related to the density of dangling-bond defect in Si materials. Under the same irradiation condition, Kr-beam irradiation is easier to produce defects, caused by displacements of atom in Si materials, than to induce remarkable change in the order of Si network.

In addition, the dip observed in *Δ*Hardness at 105 nm for 1×10^{14} ions/cm^2 and at 145 nm for 5×10^{14} ions/cm^2, corresponds with the event of pop-in in the loading-displacement curves, mentioned in section 5.1. This dip indicates the formation of a new phase by indentation process. The phase transition of a-Si induced by the indentation process was confirmed in ref. [41, 42]. Previous research [60] reported that silicon undergoes transformation from ambient-pressure diamond cubic structure (Si-I) to more dense β-Sn (Si-II) structure at pressures of 10 – 13 GPa. This semiconductor transformation is accompanied by a volume reduction of 22 % [61]. Ruffell *et al.*[62] provided a model to understand the phase transition with different loading speed and the region of phase transition is beneath the tip of nano-indenter. Therefore, during the penetration of the tip in a-Si, this transformed region moves towards deeper region. According to Fig. 5-5, the thickness of amorphous layers are 199 and 240 nm for the fluence of 1×10^{14} and 5×10^{14} ions/cm^2, respectively. When the transformed region reaches the boundary between a-Si and c-Si, it is expected that the displacement of phase transition region is confined so the accumulation of extra stress results in the hardness increase, which can be confirmed by the additional decrease in *Δ*Hardness, shown in Fig. 5-3(b), in the depth range of 60–105 nm for the curve of 1×10^{14} ions/cm^2 and 95 – 145 nm for the curve of 5×10^{14} ions/cm^2. Furthermore, the c-Si, which is located beneath the boundary, would undergoes transformation at a pressure of 12.5 ~ 13.2 GPa, shown in Fig. 5-2(b), which corresponds to

the reported pressure, 10- 13 GPa, from Si-I phase to Si-II phase [60]. Corresponding event of pop-in was observed in loading-displacement curve because of the volume reduction [61]. Based on the above argument, the dip phenomena observed for hardness can be considered to originate from the phase transition of c-Si induced by indenter in the loading process.

5.6.3 The application of depth profile of mechanical properties

In this section, I will discuss about the possibility of application of depth profile of modified mechanical properties. Based on previous discussion, the depth profile of modified mechanical properties can be applied as a new index to determine the size of the transformed region during the loading process. According to ref [41], metallic Si-II phase induced by nanoindentation is unstable at the pressure below 2 GPa, the material undergoes further transformation to different phase, such as an *a*-Si phase or polycrystalline phases (Si-III and Si-XII), during the press release. Therefore, it is little chance to evaluate the size of metallic Si-II phase after unloading. Based on discussion in previous section, the dip found in the depth profile of *Δ*Hardness would be understand based on interaction between transformed region and the boundary between *a*-Si and *c*-Si. Assuming this idea, it is considered that the boundary of phase transition region induced by nano-indentation has reach the interface between amorphous and crystalline Si when tip of nano indenter reaches a depth of 60 nm. Fig. 5-5 shows that the thickness of amorphous layer is 199 nm. Then, the longitudinal size of the phase transition region is estimated about 139 nm. Applying same method, the longitudinal size of 145 nm is estimated for 5×10^{14} ions/cm^2. These consistent results indicate a potential application and also provide the longitudinal size of phase transition region induced by nanoindentation.

In addition, the sensitivity of Young's modulus to the amorphous phase can be applied, as a potential technology, to determine the thickness of the amorphous layer by continuous measurement in nanoindentation method.

5.7 Conclusion on modification of mechanical properties

The nanoindentation measurements have been performed on *c*-Si irradiated by a Kr-ion

beam with the energy of 240 keV to evaluate the effect of irradiation on mechanical properties. The observed results has shown changes in mechanical properties increases with the fluence. In addition, the hardness is more sensitive to the damage induced by ion beam irradiation than the Young's modulus. The fluence dependence of Young's modulus can be understood by the decrease in the order of Si network induced by ion beam irradiation. On the other hand, the fluence dependence of hardness is ascribed to the induced increase of defects caused by ion beam irradiation. The different response of mechanical properties to damage induced by ion beam irradiation are ascribed to their different mechanism of modification. In addition, a possibility of a new method to determine the longitudinal size of transformed region was proposed.

6 Conclusion

In this thesis, I studied about modification of morphologies and mechanical properties of Si crystal. Deformation of nanostructures along the lateral direction indicated the fine controllability of lateral size of structures on *c*-Si surface by introducing expansion effect with low fluence ion-beam irradiation. In addition, modification of mechanical properties exhibited the reduction of mechanical properties. However, the reduction is not so serious under condition of low-fluence ion-beam irradiation compared with that of amorphous materials. The main results are summarized as following:

1 Observed lateral deformation depends on the lateral size of stripe structure as well as the fluence of Kr beam. The typical fluence of 240 keV Kr-beam, employed to provide lateral deformation, is about 1 x 10^{14} ion/cm^2. This fluence is much lower than the typical fluence of ion beams, which is needed to provide plastic deformation in amorphous materials.

2 A consistent qualitative explanation for observed lateral deformation and its fluence dependence was provided based on the amorphous/crystalline pockets and CLIB model. The suppression effect on the lateral deformation, which would be originated from crystalline region between two interfaces in the center pile, provides a possible explanation for the structure size dependence. However, further investigations are needed to confirm the reliability of this idea.

3 Observed changes in mechanical properties depend on the fluence. The fluence dependence of Young’s modulus can be understood by the decrease in the order of Si network induced by ion beam irradiation. On the other hand, the fluence dependence of hardness is ascribed to the increase of defects induced by ion beam irradiation.

4 The hardness is more sensitive to the damage induced by ion beam irradiation than the Young’s modulus. The different response of modified mechanical properties to damage induced by ion beam irradiation are ascribed to their different sensitivity to the type of defects.

5 A new method to determine the longitudinal size of transformed region was proposed.

In conclusions, lateral deformation of surface nanostructures on *c*-Si indicated fine possibilities in the field of 3D micro-/nanofabrication. Modification of mechanical properties indicated the different effect on Young’s modulus and nanohardness, which provide a firmed evidence to strength this potential application.

Acknowledgement:

I would like to thank Professor S. Momota, my supervisor, for his guidance and support during my PhD period. Thank you for giving me freedom in doing research and teaching me the research methods.

All of irradiation experiments were supported by Momota-Lab colleagues. (K. Maeda, H. Fukui, H. Katou, Y. Hashimoto, S. Shinnyama, T. Yamuguchi, N. Sato, H. Tokaji)

Operation and analysis results of SEM, TEM, were helped by Dr. N. Nitta and Dr. X. LI.

Discussions and suggestions given from Prof. M. Taniwaki, Prof. M. Furuta, Prof. A. Hatta, Prof. H. Furuta, and Dr. D. Wang

I appreciate all IRC staff members to make my staying in Japan comfortable, enjoyable, and memorable.

Thanks all my friends at KUT. At last, I would like to thanks my family members.

References:

1. Gaspar, J., V. Chu, and J.P. Conde, *Amorphous silicon electrostatic microresonators with high quality factors.* Applied Physics Letters, 2004. **84**(4): p. 622-624.

2. JJ, G., et al., *A MEMS based amperometric detector for E. coli bacteria using self-assembled monolayers.* Biosensors and bioelectronics, 2001. **16**: p. 745-55.

3. Pirmoradi, F.N., et al., *A magnetically controlled MEMS device for drug delivery: design, fabrication, and testing.* Lab on a chip, 2011. **11**(18): p. 3072-80.

4. Glos, D.L., et al., *Implantable MEMS compressive stress sensors: Design, fabrication and calibration with application to the disc annulus.* Journal of biomechanics, 2010. **43**(11): p. 2244-8.

5. Cantagrel, M., *Comparison of the properties of different materials used as masks for ion‐beam etching.* Journal of Vacuum Science & Technology A, 1975. **12**(6): p. 1340-1343.

6. Lee, R.E., *Microfabrication by ion‐beam etching.* Journal of Vacuum Science & Technology A, 1979. **16**(2): p. 164-170.

7. Vasile, M.J., et al., *Focused ion beam milling: Depth control for three-dimensional microfabrication.* Journal of Vacuum Science & Technology B, 1997. **15**(6): p. 2350-2354.

8. Matsui, S., et al., *High-resolution focused ion beam lithography.* Microelectronic Engineering, 1990. **11**(1–4): p. 427-430.

9. Savvides, N., *Surface microroughness of ion-beam etched optical surfaces.* Journal of Applied Physics, 2005. **97**(5): p. -.

10. Peng, C.Y., et al., *Ideally ordered 10 nm channel arrays grown by anodization of focused-ion-beam patterned aluminum.* Journal of Vacuum Science & Technology B, 2005. **23**(2): p. 559-562.

11. Lo, C.J., T. Aref, and A. Bezryadin, *Fabrication of symmetric sub-5 nm nanopores using focused ion and electron beams.* Nanotechnology, 2006. **17**(13): p. 3264.

12. Altissimo, M., *E-beam lithography for micro-nanofabrication.* Biomicrofluidics, 2010. **4**(2).

13. van Dillen, T., et al., *Ion beam-induced anisotropic plastic deformation of silicon*

microstructures. Applied Physics Letters, 2004. **84**(18): p. 3591-3593.

14. Ruault, M.O., Fortuna, F., Bernas, H., Ridgway, M. C., Williams, J. S., *How nanocavities in amorphous Si shrink under ion beam irradiation: An in situ study.* Applied Physics Letters, 2002. **81**(14): p. 2617.

15. Danesh, P., et al., *Effect of keV ion irradiation on mechanical properties of hydrogenated amorphous silicon.* Nuclear Instruments and Methods in Physical Research Section B, 2010. **268**(17–18): p. 2660-2665.

16. Giri, P.K., et al., *Mechanism of swelling in low-energy ion-irradiated silicon.* Physical Review B: Condensed Matter, 2001. **65**(1): p. 012110.

17. Li, Y.H., et al., *Swelling effects in $Y_2Ti_2O_7$ pyrochlore irradiated with 400 keV Ne^{2+} ions.* Nuclear Instruments and Methods in Physics Research Section B, 2012. **274**(0): p. 182-187.

18. Nipoti, R., et al., *Ion implantation induced swelling in 6H-SiC.* Applied Physics Letters, 1997. **70**(25): p. 3425-3427.

19. Custer, J.S., et al., *Density of amorphous Si.* Applied Physics Letters, 1994. **64**(4): p. 437-439.

20. Momota, S.Z., Jianguo; Toyonaga, Takuya; Terauchi, Hikaru; Maeda, Kazuki; Taniguchi, Jun; Hirao, Takashi; Furuta, Mamoru; Kawaharamura, Toshiyuki, *Control of Swelling Height of Si Crystal by Irradiating Ar Beam.* Journal of nanoscience and nanotechnology, 2012. **12**(1): p. 552-556.

21. Momota, S., et al., *Control of swelling height of Si crystal by irradiating Ar beam.* Journal of nanoscience and nanotechnology, 2012. **12**(1): p. 552-6.

22. Otani, K., et al., *Three-dimensional morphology evolution of SiO_2 patterned films under MeV ion irradiation.* Journal of Applied Physics, 2006. **100**(2): p. 023535.

23. Ruault, M.-O., et al., *How nanocavities in amorphous Si shrink under ion beam irradiation: An in situ study.* Applied Physics Letters, 2002. **81**(14): p. 2617-2619.

24. van Dillen, T., et al., *Size-dependent ion-beam-induced anisotropic plastic deformation at the nanoscale by nonhydrostatic capillary stresses.* Physical Review B: Condensed Matter, 2006. **74**(13).

25. Guo, X., et al., *Lateral deformation of a silicon crystal surface structure induced by low-fluence ion-beam irradiation.* e-Journal of Surface Science and Nanotechnology,

2015. **3**.

26. Su, W.-S., W. Fang, and M.-S. Tsai. *Tuning the mechanical properties of poly-silicon film by surface modification using plasma treatment*. in *2004 MRS Spring Meeting*. 2004. Materials Research Society 2004.

27. Namazu, T., Y. Isono, and T. Tanaka, *Evaluation of size effect on mechanical properties of single crystal silicon by nanoscale bending test using AFM*. Journal of Microelectromechanical Systems, 2000. **9**(4): p. 450-459.

28. Virwani, K.R., et al., *Young's modulus measurements of silicon nanostructures using a scanning probe system: a non-destructive evaluation approach.* Smart Materials and Structures, 2003. **12**(6): p. 1028.

29. Li, X., et al., *Ultrathin single-crystalline-silicon cantilever resonators: Fabrication technology and significant specimen size effect on Young's modulus.* Applied Physics Letters, 2003. **83**(15): p. 3081.

30. Sohn, Y.S., et al., *Mechanical properties of silicon nanowires.* Nanoscale research letters, 2009. **5**(1): p. 211-216.

31. Li, X., et al., *Study on ultra-thin NEMS cantilevers - high yield fabrication and size-effect on Young's modulus of silicon*, in *The Fifteenth IEEE International Conference on Micro Electro Mechanical Systems*. 2002. p. 427-430.

32. ZHANG, J., *Mechanism and application of morphological changes of Si crystal material induced by ion-beam.* 2012.

33. Trautmann, C., et al., *Swelling of insulators induced by swift heavy ions.* Nuclear Instruments and Methods in Physics Research Section B, 2002. **191**(1–4): p. 144-148.

34. Wortman, J.J. and R.A. Evans, *Young's Modulus, Shear Modulus, and Poisson's Ratio in Silicon and Germanium.* Journal of Applied Physics, 1965. **36**(1): p. 153.

35. Pantchev, B., et al., *Effect of post-hydrogenation on the structural properties of amorphous silicon network.* Japanese Journal of Applied Physics, 2004. **43**(2): p. 454-458.

36. Pantchev, B., et al., *Nanoindentation-induced pile-up in hydrogenated amorphous silicon.* Journal of Physics: Conference Series, 2010. **253**: p. 012054.

37. Pantchev, B., et al., *The effect of structural disorder on mechanical stress in a-Si:H films.* Journal of Physics D: Applied Physics, 2001. **34**(17): p. 2589.

38. Pfanner, G., et al., *Dangling-bond defect in a-Si:H: Characterization of network and strain effects by first-principles calculation of the EPR parameters.* Physical Review B: Condensed Matter, 2013. **87**(12).

39. Smith, Z.E. and S. Wagner, *Intrinsic dangling-bond density in hydrogenated amorphous silicon.* Physical Review B: Condensed Matter, 1985. **32**(8): p. 5510-5513.

40. Roorda, S., et al., *Structural relaxation and defect annihilation in pure amorphous silicon.* Physical Review B: Condensed Matter, 1991. **44**(8): p. 3702-3725.

41. Haberl, B., et al., *Phase transformations induced in relaxed amorphous silicon by indentation at room temperature.* Applied Physics Letters, 2004. **85**(23): p. 5559.

42. Ctvrtlik, R., J. Tomastik, and V. Ranc, *Nanoindentation-induced phase transformation in silicon thin films.* Key Engineering Materials, 2014. **586**: p. 112-115.

43. Danesh, P., et al., *Effect of hydrogen on hardness of amorphous silicon.* Applied Physics A, 2010. **102**(1): p. 131-135.

44. Yu, J., et al., *TEM investigation of FIB induced damages in preparation of metal material TEM specimens by FIB.* Materials Letters, 2006. **60**(2): p. 206-209.

45. ZHANG, J., *Mechanism and application of morphological changes of Si crystal material induced by ion-beam*, in *Department of Mechanical Systems Engineering*. 2012, Kochi University of Technology: Kami-city. p. 102.

46. Sadao Momota, Y.N., Miwako Saihara, Asako Sakamoto, Hisayoshi Hamagawa, and Kensuke Hamaguchi *First operation of ECR ion source at Kochi University of Technology.* Review of Scientific instruments, 2004. **75**(5).

47. Oliver, W.C. and G.M. Pharr, *Measurement of hardness and elastic modulus by instrumented indentation Advances in understanding and refinements to methodology.* Journal of Materials Research, 2004. **19**(01): p. 3-20.

48. Oliver, W.C. and G.M. Pharr, *An improved technique for determining hardness and elastic modulus using load and displacement sensing indentation experiments.* Journal of Materials Research, 1992. **7**(6): p. 1564-1583.

49. J.F. Ziegler, J.P.B., M.D. Ziegler, *The Stopping and Range of Ions in Matter*, in *Treatise on Heavy-Ion Science*. 1985, Springer US. p. PP 93-129.

50. Droz, C., et al., *Relationship between Raman crystallinity and open-circuit voltage in microcrystalline silicon solar cells.* Solar Energy Materials and Solar Cells, 2004. **81**(1): p. 61-71.

51. Atwater, H.A., J.S. Im, and W.L. Brown, *Heterogeneous amorphization of Si during ion irradiation: dependence of amorphous Si nucleation kinetics on defect energy and structure.* Nuclear Instruments and Methods in Physics Research Section B: Beam Interactions with Materials and Atoms, 1991. **59–60, Part 1**(0): p. 386-390.

52. Romano, L., et al., *Amorphization of Si using cluster ions.* Journal of Vacuum Science & Technology B, 2009. **27**(2): p. 597-600.

53. Trinkaus, H. and A.I. Ryazanov, *Viscoelastic Model for the Plastic Flow of Amorphous Solids under Energetic Ion Bombardment.* Physical Review Letters, 1995. **74**(25): p. 5072-5075.

54. Yoshiie, T., et al., *Effect of cascade localization induced bias on defect structure evolution.* Journal of Nuclear Materials, 1991. **179–181, Part 2**(0): p. 954-957.

55. Follstaedt, D.M., J.A. Knapp, and S.M. Myers, *Mechanical properties of ion-implanted amorphous silicon.* Journal of Materials Research, 2004. **19**: p. 338-346.

56. Bhushan, B. and X. Li, *Micromechanical and tribological characterization of doped single-crystal silicon and polysilicon films for microelectromechanical systems devices.* Journal of Materials Research, 1997. **12**(01): p. 54-63.

57. Nastasi, M., j.W. Mayer, and Y. Wang, *Ion Beam Analysis Fundamentals and Applications*. 2014, Boca Raton: CRC Press Tay & Francis Group. 460.

58. Chu, W.-K., J.W. Mayer, and M.-A. Nicolet, *Backscattering Spectrometry*. 1978, New York: Academic Press. INC. 384.

59. Szabadi, M., et al., *Elastic and mechanical properties of ion-implanted silicon determined by surface-acoustic-wave spectrometry.* physical Review B: Condensed Matter, 1998. **58**(14): p. 8941-8948.

60. Kailer, A., Y.G. Gogotsi, and K.G. Nickel, *Phase transformations of silicon caused by contact loading.* Journal of Applied Physics, 1997. **81**(7): p. 3057.

61. Domnich, V. and Y. Gogotsi, *Phase tansformations in silicon under contact loading.* Reviews on Advanced Materials Science, 2002. **3**(1): p. 1-36.

62. Ruffell, S., et al., *Identification of nanoindentation-induced phase changes in silicon by in situ electrical characterization.* Journal of Applied Physics, 2007. **101**(8): p. 083531.

63. Ben Streetman, S.B., *Solid State Electronic devices* 2005: p. 608.

Publications:

X. GUO, S. MOMOTA, N. NITTA, K. MAEDA, Lateral deformation of a silicon crystal surface structure induced by low-fluence ion-beam irradiation, e-J. Surf. Sci. Nanotech., 3 (2015).

X. GUO, S. MOMOTA, N. NITTA, T. YAMAGUCHI, N. SATO, H. TOKAJI, Modification of mechanical properties of Si crystal irradiated by Kr-beam, Applied Surface Science, (submitted)

International conference

The 11th European Conference on Accelerators in Applied Research and Technology , Sep. 08-13, 2013,Namur, Belgium (Oral)

ICSOS-11th International Conference on the Structure of Surfaces, 21-25 July 2014, University of Warwick, Coventry, UK (Poster)

APPENDIX:

The Miller Indices h, k, l are defined as follows:

(1) Place the unit cell of Figure 1 on an x, y, z Cartesian coordinate system with a lower corner atom at the origin.

(2) To define the (h k l) plane, first identify the three intercepts of the plane with the crystal axes (x, y, z). Each separation of one lattice constant, a, is given the value of 1. Planes beyond the unit cell being associated with integers greater than 1. Positive and negative integers are appropriately defined.

(3) Take the reciprocal of the three intercept integer values (1/x, 1/y, 1/z).

(4) Reduce these fractions to the smallest set of common integers (h, k, l)

For example, the top of the unit cell shown in Figure 2-2 defines the (001) plane, while the front surface is the (100) plane. Diagonals include the (111) and (110) planes. The set of {100}, {111}, and {110} form the primary planes. Surfaces tipped small angles from the primary planes are considered vicinal surfaces, while planes such as (511) and (711) are high index planes. For example the plane having the intercepts 3, 1, 1 is the (133) surface, and the direction normal to this surface is the [133]. While, the plane having the intercepts –1,-1,-1 is the (-1,-1,-1) surface. Typically, and regularly, the minus sign is placed above the miller index. Si wafers are commonly manufactured with the (100), (110) or (111) surface or flat orientations.

Inspection of the unit cell shows cell shows 6 identical and symmetric {100} planes that form the sides of the cubic structure. Similarly there are identical {111} and {110} surfaces within the cell. Although these surfaces are different relative to each other mathematically, they are indistinguishable in reality, and are chemically and physically equivalent. Therefore, the following guidelines[63] are used to define planes and directions.

(1) Use the [] notation to identify a specific direction (i.e. [1, 0, -1]).

(2) Use the <> notation to identify a family of equivalent directions (i.e. <1 1 0>).

(3) Use the () notation to identify a specific plane (i.e. (1 1 3)).

(4) Use the { } notation to identify a family of equivalent planes (i.e. {3 1 1}).